MOLECULAR DYNAMICS SIMULATION STUDIES OF MATERIAL MODIFICATION BY CHARGED PARTICLE IRRADIATION

By

INKOOK JANG

A DISSERTATION PRESENTED TO THE GRADUATE SCHOOL
OF THE UNIVERSITY OF FLORIDA IN PARTIAL FULFILLMENT
OF THE REQUIREMENTS FOR THE DEGREE OF
DOCTOR OF PHILOSOPHY

UNIVERSITY OF FLORIDA

2004

Copyright 2004

by

Inkook Jang

ACKNOWLEDGMENTS

First, I would like to show my sincere gratitude to my advisor, Dr. Susan B. Sinnott, for her constant guidance and encouragement. Her support and instant help throughout my graduate career laid a smooth way for my studies and research work, and enabled me to achieve my goal. I am also greatly thankful to all the members in Dr. Sinnott's research group for academic discussion and cheerful talks.

Finally, I wish to express my great appreciation to my beloved parents.

TABLE OF CONTENTS

page

ACKNOWLEDGMENTS iii

LIST OF TABLES vi

LIST OF FIGURES vii

ABSTRACT ix

CHAPTER

1 GENERAL INTRODUCTION 1

1.1 Molecular Simulations 1
1.2 Molecular Dynamics Method 5
1.3 Plasma Processing 7
1.3.1 Plasma Modification of Polymer 8
1.3.2 Fluorocarbon Plasma 8
1.3.3 Polyatomic Ion Deposition 9
1.4 Carbon Nanotubes Junctions 10
1.4.1 Carbon Nanotubes 10
1.4.2 Joining of Carbon Nanotube 14

2 SIMULATION METHODS 16

2.1 The Reactive Empirical Bond Order Potential 16
2.2 C-H-F Potential 19
2.3 The Lennard-Jones Potential 23
2.4 Periodic Boundary Conditions 24
2.5 Predictor-Corrector Algorithms 25
2.6 Temperature Control Methods 26
2.7 Tight Binding Methods 28

3 POLYATOMIC ION BEAM DEPOSITION ON POLYMER SURFACES 29

3.1 Simulation Details 31
3.1.1 Continuous Fluorocarbon Ion Deposition on PS Surface 32
3.1.2 Hydrocarbon Ion Deposition on PS and PE surfaces 34
3.2 Results and Discussion 34

3.2.1 Continuous Fluorocarbon Ion Deposition on PS 34
3.2.2 Angular Influence of $C_3H_5^+$ Ion Deposition on PS Surface 52
3.2.3 Polystyrene vs. Polyethylene 59
3.3 Conclusions 67
3.3.1 Continuous Fluorocarbon Ion Deposition on PS 67
3.3.2 Angular Influence of $C_3H_5^+$ Ion Deposition on PS Surface 68
3.3.3 Polystyrene vs. Polyethylene 68

4 CARBON NANOTUBE WELDING UNDER ELECTRON BEAM IRRADIATION 70

4.1 Simulation Details 70
4.2 Results and Discussion 75
4.3 Conclusions 86

5 GENERAL CONCLUSIONS 88

LIST OF REFERENCES 91

BIOGRAPHICAL SKETCH 101

LIST OF TABLES

Table page

2-1. Two-body parameters used in equation (2-2), (2-3), (2-4), and (2-6). 20

2-2. Values of P from equation (2-13) at the integer points used for cubic spline interpolation. 21

2-3. Atomization energies of various molecules calculated by new C-H-F potential and semi-empirical (PM3) method. 22

2-4. Lennard-Jones parameters. 23

3-1. Surface density of indicated species that remain bonded to carbon atoms in, or are embedded within, the PS surfaces after $C_3F_5^+$ deposition. 38

3-2. Surface density of indicated species that remain bonded to carbon atoms in, or are embedded within, the PS surfaces after CF_3^+ deposition. 38

3-3. Yield of scattering species for CF_3^+ deposition. 41

3-4. Yield of scattering species for $C_3F_5^+$ deposition. 41

3-5. Surface density of indicated species that remain bonded to carbon atoms in, or are embedded within, the PS surfaces after 105 $C_3F_5^+$ deposition at 100 eV/ion. 51

3-6. Surface density of indicated species that remain bonded to carbon atoms in, or are embedded within, the PS surfaces after 105 $C_3F_5^+$ deposition at 50 eV /ion. 51

3-7. Percentage of occurrence of the indicated events averaged over 80 trajectories at different incident angles. 53

3-8. Percentage of occurrence of the indicated events in the MD simulations of $C_3H_5^+$ deposition averaged over 80 trajectories. 60

4-1. The dimensions of each CNT pair and irradiation area. 74

4-2. Summary of bonding at the junctions formed between the following pairs of CNTs by electron beam irradiation as described in the text. 79

LIST OF FIGURES

Figure page

1-1. The scheme to determine Bravais vector. 11

1-2. Structure models of carbon nanotubes. 12

2-1. Schematic representation of periodic boundary condition. 24

2-2. Schematic diagram of typical heat bath application. 27

3-1. Models of (a) PS and (b) PE chains.. 31

3-2. Schematic representation of initial PS substrate. 33

3-3. Structure models of PS surfaces and depth profile of F density after ion beam deposition at 50 eV/ion. 35

3-4. Snapshot form the MD simulations that shows a CF_2 fragment linking two PS chains. 40

3-5. F uptake and total deposition yield of F as function of fluence during deposition. ..42

3-6. Degree of PS surface etching during ion beam deposition. 44

3-7. Average penetration depths of indicated species in the PS surfaces. 46

3-8. A portion of the PS structure after deposition of 240 $C_3F_5^+$ ions. 47

3-9. Structure models of part of the PS surfaces after 105 $C_3F_5^+$ ion deposition at 50 eV/ion and 100 eV/ion. 48

3-10. Structure models of PS surfaces and depth profiles of F density after 105 $C_3F_5^+$ ion deposition 49

3-11. Percentages of the indicated product species that remain bonded to carbon atoms in the PS surface or are embedded in the PS surface.. 55

3-12. Snapshot from the MD simulations showing the products of the dissociation of the $C_3H_5^+$ ion into CH_2 fragments that bond to the PS surface.. 57

3-13. Average number of broken bonds per trajectory in the PS surface as a result of $C_3H_5^+$ deposition at the indicated angles over the 80 trajectories. 58

3-14. Average penetration depths of major species (C_3H_5, C_2H_n, CH_2) from the incident ions as a function of angle. 59

3-15. Percentages of the indicated product species that remain bonded to carbon atoms in, or are embedded within, the PS and PE surfaces at 50 and 25 eV. 63

3-16. Average number of broken bonds in the PS and PE surfaces per MD trajectory as a result of $C_3H_5^+$ deposition at 50 and 25 eV. 65

3-17. Average penetration depths of major species (C_3H_5, C_2H_n, CH_2) from the incident ions. 67

4-1. Initial configuration of crossed nanotubes for electron beam irradiation. 72

4-2. Final structure of each CNT pair after electron beam irradiation and annealing. 76

4-3. Structure models of (a) ideal (5,5)-(5,5) CNT junction and (b) hydrogen terminated (5,5)-(5,5) CNT junction. 80

4-4. The change in energy as a function of strain during the deformation of welded CNT pairs after annealing. 81

4-5. DOS (full curve) and eigenvalue participation ratio (histogram) around the Fermi level (shifted at $E = 0$) for ideal (5,5)-(5,5) CNT junction. 83

4-6. DOS and eigenvalue participation ratio around the Fermi level for (5,5)-(5,5) CNT junction produced by electron beam irradiation. 84

4-7. Plot of the longitudinal distribution of the electron probability density for the first few eigenvalues (n=0,...8) above the Fermi level (n=0) of the (5,5)-(5,5) CNT junction produced by electron beam irradiation. 85

Abstract of Dissertation Presented to the Graduate School
of the University of Florida in Partial Fulfillment of the
Requirements for the Degree of Doctor of Philosophy

MOLECULAR DYNAMICS SIMULATION STUDIES OF MATERIAL MODIFICATION BY CHARGED PARTICLE IRRADIATION

By

Inkook Jang

May 2004

Chair: Susan B. Sinnott
Major Department: Materials Science and Engineering

Charged particle irradiation processes, such as ion beam deposition and electron beam irradiation are often used to modify the properties of various materials. However, detailed reaction mechanisms that lead to structural changes in the substrates are difficult to determine experimentally, as primarily indirect information is obtained using experimental methods. Computer simulation methods are complementary to experimental approaches and are able to provide insight into the way in which the system reaches its final state.

In these studies, molecular dynamics simulations are used to investigate polyatomic ion beam deposition on polymer surfaces and carbon nanotube welding under electron beam irradiation. The interatomic forces in the simulations are determined using the reactive empirical bond order potential for short-ranged covalent interactions and the Lennard-Jones potential for long-range van der Waals interactions. For hydrocarbon ion deposition, some inclined angles are found to be more efficient for the deposition of the

precursors necessary for polymer thin-film growth than normal incidence deposition. Also, incident energies of 50 eV/ion are predicted to be more efficient than 25 eV/ion, and polystyrene (PS) substrates facilitate the growth of hydrocarbon thin films more than does polyethylene.

In studies of fluorocarbon ion deposition, the simulations show how and why CF_3^+ and $C_3F_5^+$ play different roles in low-energy plasma deposition processes on PS. CF_3^+ ions dissociate more readily on impact and the large number of F atoms that are produced form covalent bonds with the PS chains, which both efficiently fluorinates the PS and slows down thin film growth. In contrast, $C_3F_5^+$ ions produce more fluorocarbon polymer film precursors that enhance thin film growth, while at the same time fluorinating the surface at a slower rate.

In the study of carbon nanotube welding, the structure of the generated junctions is characterized by a large degree of bonding disorder that leads to lower strength and higher ductility than those characterizing "ideal" junctions. The generated junctions also operate as quantum dots, in contrast to the ohmic behavior of ideal junctions.

CHAPTER 1
GENERAL INTRODUCTION

1.1 Molecular Simulations

Computer simulation has been a unique tool to obtain precise answers for the problems that cannot be solved analytically. Most phenomena in nature are expressed in terms of equations that cannot be solved analytically. For example, it is impossible to solve the motion of more than two interacting bodies.[1] Although it is theoretically possible to find analytical answer sometimes, computer simulation is often a more efficient method to predict the properties of the systems with complicated characteristics, such as non-linearity, lack of symmetry and a large number of degrees of freedom. Before the advent of computer simulation, the only way to predict the properties of material systems was to use approximate theories, such as the van der Waals equation in dense gases and the Bernoulli equation in fluid flow. However, those theories can be applied only to certain limited cases and often disagree with experimental results because they are over-simplified and do not explicitly describe the interaction among the basic elements like atoms or molecules. Even if a decent model that accurately describes interatomic or intermolecular interaction were devised, it would be impossible to use the model to predict the properties of real material systems without the aid of a computer. Therefore, it was very difficult to check the validity of such fundamental theories in real material systems.

At present, one of the most important roles of computer simulations is to bridge the gap between theory and experiment. For example, quantum mechanics is being widely

used to predict the various properties of materials in computer simulation. These simulation results can be directly compared with experimental results and provide essential information that cannot be obtained from experiment.

In some areas, computer simulation is the only tool available to investigate the properties and behavior of the systems. For example, shock wave propagation in solid materials is difficult to explore with experimental method because its reaction time is extremely short. For other systems at extreme temperatures or pressures, computer simulation is also often the only practical method for study. Computer simulation can create and investigate hypothetical situations and there are no limitations in setting conditions, unlike real experiments.

In molecular simulations, two most commonly used techniques are Monte-Carlo (MC) and molecular dynamics (MD) methods. MC method is more efficient than MD for finding the equilibrium structure and the most thermodynamically stable configuration. However, the MC method does not provide the dynamic properties of material systems because there is no concept of time. In the MC algorithm, each particle tries to find more a stable place by trial and error, and the whole system approaches the most stable configuration step by step. The typical procedure of MC simulation is:

1. Read coordinates of system and simulation conditions. (e.g. temperature, total number of steps, and boundary condition)
2. Calculate total potential energy of system *E*.
3. Trial move: Select a particle at random and give the particle a random displacement.
4. Calculate new total potential energy of system *E'*.

5. If $e^{-\frac{(E'-E)}{k_B T}}$ is larger than a randomly chosen number between 0 and 1, trial move is accepted. If not, discard trial move and the energy E'. (k_B is Boltzmann constant and T is temperature)

6. Repeat step 3-5 until the system reaches equilibrium.

In contrast, MD simulation provides information on both transport and equilibrium properties because it tracks the evolution of the system with time.[2-8] This means that MD methods can follow reaction mechanisms in molecular systems in "real time". However, MD methods require more computational resources than MC methods in most cases. In MC methods, only the potential energy needs to be calculated at each step, while the force acting on each particle needs to also be calculated in MD simulations.

Generally, the accuracy and validity of computer simulation is determined by the base theory used to calculate interatomic or intermolecular potential. Quantum mechanics methods are known to be the most theoretically rigorous for the description of material properties. However, it is impossible to apply complete quantum mechanics to systems that consist of many particles even with modern computers. Therefore, many approximation theories have been developed for practical use, and these theories can be categorized as first principle and semi-empirical methods. First principle methods, such as *ab-initio* Hartree-Fock based methods and density functional theory (DFT), are purely quantum mechanical and no empirical parameters are required.[9] They can model almost any type of atom without any external parameters. However, first principle methods require extremely high computational resources. Therefore, there is severe limitation of system size. Semi-empirical methods, such as AM1, PM3, MNDO, and tight-binding methods require less computational effort than first principle methods because they utilize some empirical components in addition to some quantum mechanical components

to improve computational efficiency.[10] Usually, the core electrons are not included in the calculation and only minimal basis sets are used (basis set is a set of functions used to describe the shape of the orbitals in an atom). In order to correct for the errors introduced by omitting part of the quantum mechanical theory in the calculation, empirical parameters are included. These parameters are determined by fitting the results to experimental data or *ab-initio* calculations. Generally, semi-empirical methods require different parameters for different atom or molecule types.[10]

In many cases, however, semi-empirical methods are still too computationally expensive for the study of large systems. For this reason, empirical methods have been developed for the study of relatively large systems, such as polymers and proteins. Unlike first principles or semi-empirical methods, empirical methods do not use wave functions or electron densities, but instead use explicit functions fitted to specific kinds of interatomic or intermolecular interactions. Due to this simplicity, empirical methods are generally much faster and can treat larger system than first principles or semi-empirical methods. One of the most popular empirical methods is molecular mechanics. In molecular mechanics, the energy of a system is expressed as the sum of several simple equations. These equations describe various aspects of the molecules, such as bond stretching, bond bending, torsion, electrostatic interactions, van der Waals forces, and hydrogen bonding. The constants in these equations are obtained from experiments or *ab-initio* calculations. However, the energies calculated in molecular mechanics are usually conformational energies so that the actual value of energy has no physical meaning. In addition, molecular mechanics methods are not applicable to structures which are far from equilibrium. Therefore, molecular mechanics are unable to predict transition states

or allow for bond breaking or new bond formation. In spite of these limitations of molecular mechanics methods, they have been widely used in biochemistry because they are able to model enormous molecules, such as proteins and DNA.[10]

1.2 Molecular Dynamics Method

The MD method was first introduced by Alder and Wainwright in the late 1950's to study the interactions of hard spheres.[11,12] That study provided many important insights about the behavior of simple liquids. The first MD simulation of a realistic system was performed by Rahman and Stillinger with liquid water system in 1974.[13] Since then many simulation techniques have been developed and MD methods have became crucial tools in many areas, such as materials science, chemistry, biology, and pharmacology.

MD simulations are very similar to real experiments in many respects.[1] First, a model system consisting of N particles is built. Then, Newton's equations of motion for this system are solved until the properties of the system no longer change with time. Finally, a measurement is performed on this equilibrated system. Unlike MC simulations, MD simulations can also provide detailed information about how the system evolves during the process. Because of this, the results of MD simulations can be directly compared with real experiments in most cases.

The general procedure for MD simulation is :

1. Set up the simulation condition. (e.g. temperature, total number of steps, boundary condition, and time step)
2. Initialize the system (positions, velocities, accelerations, etc.)
3. Compute the forces on every particle.
4. Integrate Newton's equations of motion. This step is repeated for total number of steps.

As mentioned above, MD simulation methods are based on Newton's second law of motion,

$$F_i = m_i a_i \tag{1-1}$$

where F_i is the force exerted on particle i, m_i is the mass of particle i and a_i is the acceleration of particle i. The force can also be expressed as the gradient of the potential energy.

$$F_i = -\nabla_i V \tag{1-2}$$

Therefore, acceleration can be calculated from the potential energy. Integration of the equation of motion yields a trajectory that predicts the positions, velocities, accelerations, and higher order of derivatives if they are needed, as the system varies with time. From this trajectory, average value of properties can be determined at any time.

As mentioned above, there is no analytical solution for the equation of potential energy of the many particles system. This equation of potential energy should be solved numerically. Many numerical algorithms have been developed for integration of the equation of motion, such as Verlet, leapfrog, velocity-Verlet and predictor-corrector algorithms.[1] Algorithms such as the Verlet, leapfrog, and velocity-Verlet are adequate in most cases, but their accuracy is limited because they consider only up to the second derivative of the particle coordinate, or acceleration. Energy conservation of these algorithms is not good for long time steps (Δt). Higher order algorithms have very good energy conservation for short time simulations and make it possible to achieve higher accuracy for the same time step than Verlet-style algorithms. However, there are shortcomings to higher order algorithms. They require more computer resources and have

overall energy drifts for long time simulation. In contrast, Verlet style algorithms have little long-term energy drift.[1]

1.3 Plasma Processing

Plasma processing is widely used for surface modification and the deposition of thin films. It is efficient because it is possible to confine the effects to a depth on the order of nanometers and modification is fairly uniform over the whole surface. In addition, the use of gas plasma is environmentally friendly and can avoid the problems encountered in wet chemical techniques such as the disposal of residual solvents. Plasma processing can alter the chemical and physical properties of the treated surface in a significant manner and result in a range of new surface properties. Therefore, it is widely used to coat or manufacture biomedical devices, semiconducting devices, optical devices, contact lenses, and chemical sensors.[2,3,14-18]

Plasma can be defined as a gas containing charged and neutral species, such as electrons, positive ions, negative ions, radicals, atoms, and molecules. Plasma used in surface modification process is usually produced by glow discharge. When a small amount of gas is introduced into an evacuated chamber under high electric fields, a visible glow discharge is generated. In the glow discharge, there are numerous collision processes including ionization, excitation, dissociation and attachment, which radiate visible light. These collision processes are initiated and sustained by electron detachment. Under high enough electric fields, the atoms or molecules are ionized and free electrons and ions are generated. These charged particles are accelerated under the electric field and can collide with other atoms or molecules. By these collisions, new charged particles are generated, and cascade processes follow.[19]

1.3.1 Plasma Modification of Polymer

Plasma treatment of polymer materials can be classified into three categories: surface reaction, plasma polymerization, and etching. In surface reaction, chemical reactions occur between the gas phase species and surface materials, and various functional groups are produced and cross-linking of existing chains results. These kinds of plasma processes use gas sources of argon, ammonia, carbon monoxide, carbon dioxide, fluorine, hydrogen, nitrogen, nitrogen dioxide, oxygen, and water.[20-25] Plasma polymerization is the process that forms a thin polymer film on a surface by polymerization of an organic monomer. Typical inlet gases in plasma polymerization processes are CH_4, C_2H_6, C_2F_4, and C_3F_6. In these processes, reactions are more complex than simple surface reaction processes because the inlet gases are organic polyatomic molecules. This process involves reactions among gaseous species and reactions between gaseous species and surface materials.[26-31] Etching is the process that removes material from a surface by chemical reaction or physical sputtering. Chemical reactions produce volatile species from the surface. Oxygen plasma and fluorine containing plasmas are frequently used for etching.[32-35] In real plasma treatments, all three of these processes can occur simultaneously. By changing the operating parameters, gas feed, substrate and electrode it is possible to make one or two of these processes dominate.[19]

1.3.2 Fluorocarbon Plasma

Fluorocarbon plasmas are commonly used in several industries to chemically modify the surface properties of materials. They are used for reactive ion etching of silicon dioxide in the fabrication of semiconducting devices, and the fluorination of polymer surfaces to produce films similar to PTFE (polytetrafluoroethylene) on relatively inexpensive polymers. Fluorinated polymer surfaces have high thermal and chemical

resistance, hydrophobic properties, high dielectric constants, and low friction coefficients.[26,33,36-39] As mentioned above, surface reaction, plasma polymerization, and etching can occur simultaneously in fluorocarbon plasma. It has been reported that the tendency toward polymerization in fluorine containing plasma depends primarily on the relative concentration of CF_x, such as CF or CF_2, which are the building blocks for polymerization, with respect to F atoms. F atoms are the active species for the etching process.[40] In general, surface reaction and etching are the dominant processes in low CF_x/F ratios, whereas high CF_x/F ratios enhances polymerization. The CF_x/F ratio in plasma strongly depends on the nature of feed gas. Generally, the CF_x/F ratio increases as the ratio of C/F in feed gas increases.[19] CF_4 is widely used as feed gas for fluorination of polymer surfaces. By decomposition of CF_4, various reactive species are produced, including F, CF, CF_2, and CF_3. In CF_4 plasma, surface reaction and etching are dominant processes. However, the addition of a reducing agent, such as H_2 or C_2F_2 to the CF_4 plasma increases CF_x/F ratio and enhance polymerization because F atoms react with reducing agents and form HF or C_2F_6.[40] Instead of adding a reducing agent to CF_4 plasma, CF_3H can also be used as feed gas for fluorocarbon film growth on polymer or inorganic substrates.[41,42] The decomposition of CF_3H generates CF_3 and H, and H atoms reduce the concentration of F atoms. Therefore, the ratio of CF_x/F increases and polymerization process become dominant.

1.3.3 Polyatomic Ion Deposition

In spite of the many applications of plasma processing, there is much that is not known about the reaction mechanisms between components of the plasma and surfaces.[18,43,44] What is known is that the effects of plasma processing are highly localized to the topmost layers of the surface, and several types of particles, such as ions,

electrons, neutral atoms, and molecules, can coexist in the plasma environment. Due to this lack of understanding, it is very difficult to have good control of plasma parameters such as reactor volume and geometry, RF frequency, power level, gas flow rate, gas composition, gas pressure, and sample temperature. Although much experimental research has been done to understand plasma-surface interactions, experimental studies cannot provide direct information about the relevant reaction mechanisms. Computer simulations of plasma-surface interactions are therefore frequently used to better determine the most likely reactions.[45-47] Many different reactions are possible because many different kinds of particles are present in the system and all interact collectively with the substrate. Therefore multiple processes, such as thin-film growth and substrate etching occur simultaneously.[18,48,49] This extremely complex environment makes it difficult to realize the whole reactions in plasma even with computer simulations. To isolate the effects of polyatomic ions in low energy plasma deposition process, the deposition of mass selected polyatomic ion beams have been studied by several research groups.[2,3,48,50-53] Polyatomic ions are considered as the most important species in low-energy plasmas with regard to the modification of surface properties. Therefore, performing polyatomic ion depositions instead of plasma treatments can isolate the effects of polyatomic ions, and make it possible to better understand the dominant reactions in low-energy plasma depositions.

1.4 Carbon Nanotubes Junctions

1.4.1 Carbon Nanotubes

Carbon atoms can bond to one another in different ways to create structures with entirely different properties. Graphite and diamond, the two bulk solid phases of pure carbon, have distinctively different properties. This interesting characteristic can be

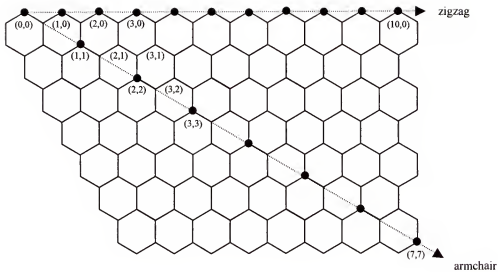

Figure 1-1. The scheme to determine Bravais vector.

attributed to the different hybridization of carbon atoms in these materials. If four valence electrons in carbon are shared equally, sp^3 hybridization, strong and transparent diamond is formed. But when only three electrons are shared covalently between neighbors in a plane and the fourth electron is delocalized among all atoms, the resulting material is graphite. This sp^2 hybridized bonding builds a layered structure with strong in-plane bonds and weak out-of-plane bonding with the van der Waals force.[54] If a single graphene, that is graphite sheet, is rolled up into a cylinder, it forms a seamless tube structure, now known as the carbon nanotube.[55] The extraordinary properties of nanotubes are attributed to this rolled up sp^2 hybridization structure. The rolling of a graphene sheet into carbon nanotube can be done in several ways, as long as dangling bonds present at both edges are matched. The manner in which the graphene sheet is rolled into a cylinder is expressed by Bravais lattice vectors. Bravais lattice vectors are defined in terms of the two primitive lattice vectors and a pair of integer indices like (n_1, n_2).[56,57] Figure 1-1 shows the scheme to determine Bravais lattice vectors. This scheme is

very important in characterizing the properties of individual nanotubes because it provides the essential symmetry of the nanotube structure, so called chirality. The (n, 0) type of nanotubes are in general called zigzag nanotubes where as the (n, n) types are called armchair nanotubes; all others will be helical.[58] Figure 2-2 shows examples of these three types of nanotubes.

In addition to chirality, carbon nanotubes can be classified as two distinct types. One is the multiwalled carbon nanotubes (MWNT) which was discovered first in 1991 by Iijima.[59] They are similar to hollow graphite fibers except that they have a much higher degree of structural perfection.[58] They consist of concentric cylinders placed around a common central hollow, with spacing between the layers close to that of the interlayer

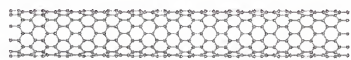

(a) (10,0)

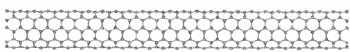

(b) (5,5)

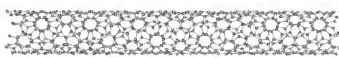

(c) (8,3)

Figure 1-2. Structure models of carbon nanotubes. (a) zigzag, (b) armchair, (c) helical

distance in graphite (0.34 nm). The second one is single-layer cylinders extending from end to end.[60,61] These are called as single-walled nanotube (SWNT). When produced in the vapor phase, the SWNT self-assemble into larger bundles (ropes) that consist of several tens of nanotubes.[62-64]

Carbon nanotubes have been one of the most widely studied materials in many scientific areas since they were discovered. Their simple but perfect structure yields some very interesting properties. For example, SWNT ropes form super strong fibers. These fibers are 100 times stronger than steel at only 1/6 of mass.[65,66] In addition to their excellent strength, SWNTs have the ability to be electrically semiconducting, conducting, or insulating. By changing their chirality, it is possible to make them as conducting as copper or an efficient semiconductor. In addition, their thermal conductivity is much higher than silicon, which suggests that they can be used to make microchips.[67-69] The chemical properties of carbon nanotubes are also exciting. The caps at both ends of carbon nanotube which are formed as they are produced can be removed through chemical means. The nanotubes can be filled with molecules and re-capped.[70,71] This could yield potential applications in medicine, or as the site for a catalyzed chemical reaction.

At present, computer simulation is an essential tool to enhance our understanding of the properties and detailed structures of new materials like carbon nanotubes. In the area of computational materials science and engineering, carbon nanotubes are one of the most frequently studied materials. Most of known fundamental properties of carbon nanotubes are the result of initial theoretical studies or computer simulations. Many potential applications of carbon nanotubes have been proposed, such as building blocks

of electronic devices, nano-filters, gas storage materials, nanoprobes, fibers for composites, and field emitters.[72-78]

1.4.2 Joining of Carbon Nanotube

Over the past few years, many experimental, computational, and theoretical studies of carbon nanotubes (CNTs) have been carried out with the aim of developing nanoscale devices. Due to their unique electrical properties and nanometer-scale sizes, individual CNTs are considered to be promising candidates for use as nanometer-scale wires[79-83] and properly joined single-walled CNTs could be the building blocks of various electronic devices.[79,84,85] For example, a junction formed by two CNTs, one of which is semiconducting and one of which is metallic, could act as a rectifying diode, while a multiterminal heterojunction, such as a 'Y' or 'T' junction, could work as a transistor.[86-89] In addition, quantum dot behavior has been observed in two-terminal heterojunctions.[90,91] By generating pentagon-heptagon defects in junction between different types of carbon nanotudes, a pure carbon quantum dot can be produced. Chico *et al.* have proposed this kind of quantum dot by sandwiching a metallic carbon nanotube between semiconducting nanotube barriers.[91] It has isolated localized levels of density of state and may have interesting optical and electrical applications.

There has been much research aimed at exploring the production and properties of CNT junctions.[75,88,92-102] These junctions have been made by several techniques, such as welding with electron beam irradiation, mechanical manipulation with atomic force microscopes, thermal annealing, and chemical functionalization.[103-108] For the realization of nanometer-scale electronic devices, appropriate electrical conductivity is required that is determined by the bonding of the atoms in the junction area between the two CNTs. The junction is usually composed exclusively of carbon atoms, except for some chemical

functionalization[106,107] or soldering techniques that utilize other materials.[104] Therefore, the properties of most junctions depend on whether the bonding in the joint is *sp*-, sp^2-, or sp^3-hybridized or whether it consists of secondary bonding. Unfortunately, determination of the bonding structure of carbon nanotube joints is difficult to do experimentally and the nature of the bonding is usually only inferred indirectly from the resulting properties. In contrast, computer simulations of CNT joining can provide detailed information on the atomic structure of the junction. In particular, MD simulations can monitor the evolution of atomic structure during the formation of the junction in a realistic manner.[45] For example, Krasheninnikov *et al.* performed MD simulations of ion irradiation induced CNT welding and showed how this approach could be used to solder CNTs.[109] Additionally, Terrones *et al.* used tight-binding MD simulations to study the coalescence of crossed CNTs and investigate the mechanisms responsible for the formation of the junction.[103] MD simulations are well suited to study irradiation processes, as the time scales of the collisions and energy dissipation are on the order of a few ps.[45]

CHAPTER 2
SIMULATION METHODS

2.1 The Reactive Empirical Bond Order Potential

Unlike molecular mechanics method, the reactive empirical bond order (REBO) method can model reactive systems in MC or MD simulations. It can predict transition states, new bond formation, and bond breaking which are important processes in material modification.

The REBO potential which was originally developed by Tersoff to describe bonding in silicon for a large number of solid state structures[110-112] was based on Abell's general expression for binding energy that is a sum of nearest neighbor pair interactions.[113] Similar expressions to the silicon system were used to model carbon and germanium systems. This expression can describe bond lengths and energies for C-C single, double, and triple bond in hydrocarbon molecules, solid graphite, and in diamond very well. It also appears to be applicable to the structures that are not used for parameter fitting, such as surface reconstruction on silicon and interstitial defects in carbon.[114] However, Tersoff's potential is unable to describe many important properties of carbon systems, such as radicals and conjugated double bonds. In order to make the potential describe those properties in hydrocarbon system realistically, Brenner introduce several new terms and parameters in Tersoff' expression.[114-116] Brenner's form of this potential has been successfully used to obtain insight into various processes such as molecular-surface collisions,[117] cluster-surface impacts,[115,118] and the chemical vapor deposition of diamond.[119]

In the REBO potential, the chemical binding energy E_b is determined using the following Equation:

$$E_b = \sum_i \sum_{j(>i)} [V_R(r_{ij}) - b_{ij} V_A(r_{ij})] \tag{2-1}$$

where $V_R(r)$ and $V_A(r)$ are pair-additive interactions that model the interatomic repulsion and attraction from electron-electron repulsion and electron-nuclear attraction, respectively. The quantity r_{ij} is the distance between pairs of nearest-neighbor atoms i and j, and b_{ij} is a bond order-term that takes into account the many-body interactions between atoms i and j, including those due to nearest neighbors and angle effects. The functions $V_R(r)$ and $V_A(r)$ are expressed as:

$$V_R(r) = f_c(r)(1 + Q/r) A e^{-\alpha r} \tag{2-2}$$

$$V_A(r) = f_c(r) \sum_{n=1,3} B_n e^{-\beta_n r} \tag{2-3}$$

where A, B, Q, α, and β are two-body parameters determined by atom type. The function $f_c(r)$ limits the range of the covalent interactions to insure that the interactions include nearest neighbors only,[116]

$$\begin{aligned} f_c(r_{ij}) &= 1 && r < D_{ij}^{\min} \\ &= [1 + \cos\{(r - D_{ij}^{\min})/(D_{ij}^{\max} - D_{ij}^{\min})\}]/2 && D_{ij}^{\min} < r < D_{ij}^{\max} \\ &= 0 && r > D_{ij}^{\max} \end{aligned} \tag{2-4}$$

where the term $D_{ij}^{\max} - D_{ij}^{\min}$ defines the distance over which the function varies from one to zero.

The bond order term is calculated using

$$b_{ij} = \frac{1}{2}[b_{ij}^{\sigma-\pi} + b_{ji}^{\sigma-\pi}] + b_{ij}^{\pi} \tag{2-5}$$

where $b_{ij}^{\sigma-\pi}$ and $b_{ji}^{\sigma-\pi}$ represent the local coordination and bond angles of atoms *i* and *j*, respectively.[116,120]

$$b_{ij}^{\sigma-\pi} = [1 + \sum_{k(\neq i,j)} f_c(r_{ik}) G(\cos(\theta_{ijk})) e^{\lambda_{ijk}\left[(r_{ij}-R_{ij}^e)-(r_{ik}-R_{ik}^e)\right]} + P_{ij}(N_i^H, N_i^C)]^{-1/2} \quad (2\text{-}6)$$

where $G(\cos(\theta_{ijk}))$ is a polynomial function and controls the influence of the nearest neighbors to the bond order according to the bond angle among atoms *i*, *j*, and *k*, and λ is a fitting parameter used to describe three-body transition states around H atoms. The function *P* is a correction term that accounts for the different chemistry around atom *i*. In particular, the values of N_i^C and N_i^H represent the number of C and H atoms, respectively, which are the nearest neighbors of atom *i*. The function *P* is not defined analytically, but the values are determined by cubic spline interpolation with some predetermined values.

The function b_{ij}^{π} in equation (2-5) has the form of

$$b_{ij}^{\pi} = \Pi_{ij}^{RC} + \Pi_{ij}^{DH} \quad (2\text{-}7)$$

Π_{ij}^{RC} describes conjugated systems and radical character between atom *i* and *j*, and Π_{ij}^{DH} depends on the dihedral angles in C-C double bonds.[116]

$$\Pi_{ij}^{RC} = Y_{ij}(N_i^t, N_j^t, N_{ij}^{conj}) \quad (2\text{-}8)$$

The values of function *Y* are determined by tricubic spline interpolation as function *P*. N_i^t and N_j^t is total number of neighboring atoms around atom *i* and *j*, respectively, regardless of their type. N_{ij}^{conj} depends on local conjugation and is expressed as

$$N_{ij}^{conj} = 1 + \left[\sum_{k(\neq i,j)}^{carbon} f_c(r_{ik}) F(x_{ik})\right]^2 + \left[\sum_{l(\neq i,j)}^{carbon} f_c(r_{jl}) F(x_{jl})\right]^2 \quad (2\text{-}9)$$

$$x_{ik} = N_k^t - f_c(r_{ik}) \tag{2-10}$$

$$F(x) = 1 \qquad x < 2$$

$$= \left[1 + \cos\left\{2\pi(x-2)\right\}\right]/2 \qquad 2 < x < 3 \tag{2-11}$$

$$= 0 \qquad x > 3$$

The term Π_{ij}^{DH} in Equation (2-7) has zero value if either of atoms i or j are not carbon. It has the form of

$$\Pi_{ij}^{DH} = T_{ij}(N_i^t, N_j^t, N_{ij}^{conj})\left[\sum_{k(\neq i,j)}\sum_{l(\neq i,j)}\left\{1-\cos^2(\Theta_{ijkl})\right\}f_c(r_{ik})f_c(r_{jl})\right] \tag{2-12}$$

where $\Theta_{ijkl} = e_{jik}e_{ijl}$ and values of function T are determined tricubic spline interpolation. The functions e_{jik} and e_{ijl} are unit vectors in the direction of the cross products $\mathbf{R}_{ji} \times \mathbf{R}_{ik}$ and $\mathbf{R}_{ji} \times \mathbf{R}_{ik}$, respectively. $\mathbf{R}_{ji}$ is vector which connect atom j and i.[116]

2.2 C-H-F Potential

In order to perform simulations of fluorocarbon ion deposition, new C-H-F potential was developed based on Brenner's REBO potential. Two-body parameters, A, B, Q, α, and β in equation (2-2) and (2-3), for C-F and F-F interactions are adapted from the potential developed by Graves and co-workers[47,121] while the H-F interaction parameters are determined from calculations using the semi-empirical AM1 approach.[122,123]

$$V_R(r) = f_c(r)(1 + Q/r)Ae^{-\alpha r} \tag{2-2}$$

$$V_A(r) = f_c(r)\sum_{n=1,3} B_n e^{-\beta_n r} \tag{2-3}$$

The functions used for $V_R(r)$ and $V_A(r)$ are the same as those used in the second generation version of the REBO potential developed by Brenner and co-workers for

hydrocarbons.[116] Some of two-body parameters are adopted from the C-H second generation REBO[116] and some are adopted from the C-F and F-F potential developed by Graves and co-workers.[47] All the parameters used here are given in Table 2-1.

The function $b_{ij}^{\sigma-\pi}$ in Equation (2-6) is modified to allow for F neighbors. The overall form of function is not changed but one new variable, N_i^F, is added for function P.

$$b_{ij}^{\sigma-\pi} = [1 + \sum_{k(\neq i,j)} f_c(r_{ik}) G(\cos(\theta_{ijk})) e^{\lambda_{ijk}[(r_{ij}-R_{ij}^e)-(r_{ik}-R_{ik}^e)]} + P_{ij}(N_i^H, N_i^C, N_i^F)]^{-1/2} \quad (2\text{-}13)$$

Table 2-1. Two-body parameters used in equation (2-2), (2-3), (2-4), and (2-6). Parameters for C-C, C-H and H-H are adopted from the second-generation REBO potential developed by Brenner and co-workers,[116] and C-F and F-F parameters are adopted from the C-F potential developed by Graves and co-workers.[47,121]

	C-C	C-H	H-H	C-F	F-F	H-F
A (eV)	10953.54416	149.940987	32.817356	909.2022	16451.97	887.0513
B_1 (eV)	12388.79198	32.355186	29.632593	219.7799	146.8149	571.1737
B_2 (eV)	17.567406	0	0	0	0	0
B_3 (eV)	30.714932	0	0	0	0	0
Q (Å)	0.313460	0.340776	0.370471	0	0	0
α (Å^{-1})	4.746539	4.102550	3.536299	3.7128	6.8149	3.7789
β_1 (Å^{-1})	4.720452	1.434458	1.715892	2.1763	2.8568	3.0920
β_2 (Å^{-1})	1.433213	-	-	-	-	-
β_3 (Å^{-1})	1.382691	-	-	-	-	-
D_{min} (Å)	1.7	1.3	1.1	1.7	1.7	1.3
D_{max} (Å)	2.0	1.8	1.7	2.0	2.0	1.8
R^e	-	1.09	0.7416	1.2718	1.4119	0.9378

For fitting parameter λ, additional values are added to consider the existence of F atom. Now, the parameter λ describes transition states around F as well as H atoms. The same λ value of 4.0 is used for F and H atoms,[116] while λ is zero for C atoms. As mentioned above, the function P is not defined analytically, but the values are determined by cubic spline interpolation with some predetermined values. In this work, some new parameters are generated for the P function to include the effect of F atoms. Values at the knots for spline interpolation are determined using the semi-empirical, AM1 method[122,123] by fitting to atomization energies of model structures, while the parameters used for the P function for hydrocarbons only is unchanged from the values in the second generation REBO potential.[116] The values used to generate the new parameter sets are given in Table 4-2.

Table 2-2. Values of P from equation (2-13) at the integer points used for cubic spline interpolation. For P_{CF}, the values not listed are equal to zero.

N^H	N^C	N^F	P_{CC}	N^H	N^C	N^F	P_{CH}	N^H	N^C	N^F	P_{CF}
0	0	2	0.00881	0	0	1	0.20934	0	0	1	0.19024
1	0	1	0.00347	0	0	2	-0.05233	0	0	2	0.34857
0	0	3	0.00191	1	0	1	-0.05912	1	0	1	0.33900
1	0	2	-0.00855	0	0	3	-0.28246	1	0	0	0.19024
2	0	1	-0.00577	1	0	2	-0.29589	2	0	0	0.32997
0	1	1	0.00341	2	0	1	-0.30337	0	0	3	-0.30393
0	1	2	-0.00030	0	1	1	-0.12567	1	0	2	-0.31297
1	1	1	-0.00068	0	1	2	-0.28383	2	0	1	-0.31401
0	2	1	0.00153	1	1	1	-0.29783	3	0	0	-0.30555
				0	2	1	-0.31230	0	1	0	0.35
								0	2	0	0.40311
								0	1	1	0.13292
								1	1	0	0.13300
								0	1	2	-0.29218
								1	1	1	-0.29100
								2	1	0	-0.27497
								0	3	0	0.06844
								0	2	1	-0.20259
								1	2	0	-0.18290

The function b_{ij}^{π} in Equation (2-7) is introduced to describe conjugated systems, radical character, and the influence of dihedral angles in C-C double bonds.[116] In this function, fluorine atom can be described as same as hydrogen atom. Therefore, the formulation of this function is unchanged from the second generation REBO and is unaffected by the addition of F.

In Table 2-3, atomization energies of various molecules calculated with new C-H-F potential are compared with the energies obtained by semi-empirical (PM3) calculation. These molecules are typical in polyatomic ion deposition.

Table 2-3. Atomization energies of various molecules calculated by new C-H-F potential and semi-empirical (PM3) method.

Molecule	C-H-F REBO (eV)	Semi-empirical (PM3) (eV)
CF_4	19.81	20.44
CHF_3	19.48	19.15
CH_2F_2	19.08	18.06
CH_3F	18.63	17.34
CF_3	14.7	15.65
CHF_2	14.28	14.63
CH_2F	13.84	13.68
CF_2	10.91	11.18
CHF	9.69	9.2
C_2F_6	33.07	33.5
$C_2H_2F_4$	32.53	31.37
$C_2H_4F_2$	31.56	29.85
C_2F_4	25.89	25.39
$C_2H_2F_2$	25.2	25.39
C_2F_2	18.27	16.69
C_6F_{12} (cyclo)	77.74	79.51
$C_6H_6F_6$ (cyclo)	76.96	74.98
C_6F_6 (cyclo)	59.44	59.3

2.3 The Lennard-Jones Potential

The Lennard-Jones (LJ) potential is the most popular form to simulate van der Waals interaction. There are several variations on the basic functional form of this potential,[10] but only the 12-6 form of the LJ potential is used throughout the simulation studies described in this dissertation. The 12-6 LJ potential is expressed as:

$$V_{LJ} = 4\varepsilon\left[\left(\frac{\sigma}{r}\right)^{12} - \left(\frac{\sigma}{r}\right)^{6}\right] \tag{2-14}$$

where σ and ε are the Lennard-Jones parameters selected for the types of interacting atoms, and r is interatomic distance. The parameters σ and ε used in these studies are shown in Table 2-4. Table 2-4 contains only the parameters for interaction between atoms of the same types. For the interaction between atoms of different types, there is a rule to determine the Lennard-Jones parameters. If the parameters for the interaction between same types of atom are expressed as σ_{AA}, and ε_{AA}, the parameters for the interaction between different atoms are determined by the equations of

$$\sigma_{AB} = \frac{1}{2}\left(\sigma_{AA} + \sigma_{BB}\right) \tag{2-15}$$

$$\varepsilon_{AB} = \sqrt{\varepsilon_{AA} \cdot \varepsilon_{BB}} \tag{2-16}$$

Table 2-4. Lennard-Jones parameters.

	σ(Å)	ε(kJ/mol)
C-C	2.28	0.426
H-H	2.81	0.0715
F-F	2.81	0.519

2.4 Periodic Boundary Conditions

For the computer simulation of solid state materials, such as the surface modification of polymers and the etching of silicon surfaces, the size of the system is extremely small compared with the system in real experiments, and the system size often influences the results. To avoid size effects and mimic an large surface area, periodic boundary conditions are usually applied to the four side directions of the slab. The concept of periodic boundary condition is shown in Figure 2-1. The volume containing the N particles is treated as the primitive cell of an infinite periodic lattice of identical cells. A given particle **A** interacts with all other particles in this infinite periodic system, that is, all other particles in the same periodic cell and all particles in all other cells. However, this makes problem that the particle may interacts with itself and it is unrealistic. In practical systems, interaction distance is limited to certain range by some kind of function like Equation (2-4). Therefore, the particle **A** interacts only with other particles within the dashed box.

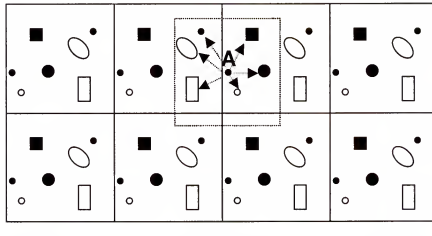

Figure 2-1. Schematic representation of periodic boundary condition.

2.5 Predictor-Corrector Algorithms

Predictor-corrector is the most popular higher order algorithm used in MD simulations. All MD simulations in these studies performed with predictor-corrector algorithms. The basic idea of the predictor-corrector algorithm is to predict the positions and first n derivatives of N particles at time t+Δt from the information about their positions and first n derivatives at time t using Taylor's expansion. For the third order algorithm, predicted position ($\vec{r}^{\,p}$), velocity ($\vec{v}^{\,p}$), acceleration ($\vec{a}^{\,p}$), and third derivative ($\vec{b}^{\,p}$) at t+Δt are expressed as :

$$\vec{r}^{\,p}(t+\Delta t) = \vec{r}(t) + \Delta t \cdot \vec{v}(t) + \frac{1}{2}\Delta t^2 \cdot \vec{a}(t) + \frac{1}{6}\Delta t^3 \cdot \vec{b}(t) \tag{2-17}$$

$$\vec{v}^{\,p}(t+\Delta t) = \vec{v}(t) + \Delta t \cdot \vec{a}(t) + \frac{1}{2}\Delta t^2 \cdot \vec{b}(t) \tag{2-18}$$

$$\vec{a}^{\,p}(t+\Delta t) = \vec{a}(t) + \Delta t \cdot \vec{b}(t) \tag{2-19}$$

$$\vec{b}^{\,p}(t+\Delta t) = \vec{b}(t) \tag{2-20}$$

At the predicted positions, forces are calculated and corrected accelerations $\vec{a}^{\,c}(t+\Delta t)$ obtained. In general, these calculated accelerations are not equal to the predicted values. This discrepancy will be used to obtain the corrected positions and remaining derivatives. The adjusting parameter ($\Delta\vec{a}$) is expressed as:

$$\Delta\vec{a}(t+\Delta t) = \vec{a}^{\,c}(t+\Delta t) - \vec{a}^{\,p}(t+\Delta t) \tag{2-21}$$

Then, the positions and remaining derivatives will be corrected as follows:

$$\vec{r}^{\,c}(t+\Delta t) = \vec{r}^{\,p}(t+\Delta t) + C_0\Delta\vec{a}(t+\Delta t) \tag{2-22}$$

$$\vec{v}^{\,c}(t+\Delta t) = \vec{v}^{\,p}(t+\Delta t) + C_1\Delta\vec{a}(t+\Delta t) \tag{2-23}$$

$$\vec{b}^{\,c}(t+\Delta t) = \vec{b}^{\,p}(t+\Delta t) + C_3\Delta\vec{a}(t+\Delta t) \tag{2-24}$$

where C_n are constants optimized for a given order algorithm. For example, $C_0 = \frac{1}{6}$, $C_1 = \frac{5}{6}$, $C_2 = 1$, and $C_3 = \frac{1}{3}$ for the third order Nordsieck predictor-corrector algorithm.[124] These corrected values are used to predict the positions and first n derivatives at the next step, and then the same procedure is repeated.

Although higher orders of the predictor-corrector algorithm are supposed to give more accurate results, the accuracy improvement becomes less significant as the order of the algorithm increases because the error of nth order algorithm is on the order of Δt^n. In contrast, the accuracy of the trajectory is more sensitive to the length of the time step than the order of the high order algorithm.[1] The time step should be determined to obtain an optimal compromise between accuracy and simulation time. In highly dynamic systems, short time steps should be used. The simulation will predict unphysical results if the time step is not short enough. For less dynamic systems, relatively longer time steps can be used.

2.6 Temperature Control Methods

In the basic version of MD simulation, the system has a constant number of particles (N), volume (V) and energy (E) because the total energy should be conserved in the closed system which follows Newton's equation of motion. Therefore, MD simulations measure time average properties in the microcanonical (constant NVE) ensemble. However, in many cases, it is required to perform simulation at constant system temperature (T) because most real experiments are done in the condition of constant temperature. In this case, the average properties are measured in the canonical (constant NVT) ensemble.

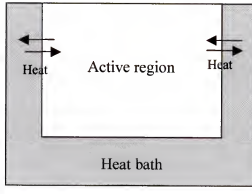

Figure 2-2. Schematic diagram of typical heat bath application.

In order to perform MD simulations at constant temperature, the system is brought into thermal contact with a large heat bath. Schematic diagram of typical heat bath application is shown in Figure 2-2. In Figure 2-2, atoms in active region follow Newton's equation of motion without any restriction. The temperature of heat bath is virtually constant. There are several schemes, such as velocity scaling, Andersen, Nosé-Hoover and Langevin thermostats, to control the motion of atoms in heat bath region to attain desired temperature. Here, only the Langevin thermostat will be considered because Langevin thermostat is used to control the system temperature for all MD simulations in these studies.

The atoms in heat bath region follow the Langevin Equation of motion instead Newton's equation of motion. It is expressed as

$$ma = F - \beta v + F' \tag{2-25}$$

where m is mass of atom, a is acceleration, F is force acting on atom, v is the velocity of atom, β is a frictional constant, and F' is a stochastic force. The effect of frictional force - βv is decrease the temperature because β is fixed as positive value for a given structure.

The stochastic force is randomly determined from a Gaussian distribution, and its variance is a function of the desired temperature and time step. Therefore, the stochastic force is balanced with frictional force and maintains the system temperature.[124]

2.7 Tight Binding Methods

The tight binding method is one of several semi-empirical calculation methods that model only valence orbitals based on the orbital overlaps, experimental electron affinities and ionization potentials.[10] There are various types of tight binding methods,[125-131] and not all of them are as accurate or sophisticated method compared with other semi-empirical methods, such as AM1 and PM3. However, they are usually general enough to model all the elements in the periodic table and are often used to study for inorganic materials because they are faster than Hartree-Fock based methods and DFT.

Tight binding methods are very useful for computing band structures, which are extremely computation-intensive calculations. In addition, they provide a very convenient way to view orbital symmetry.[10]

CHAPTER 3
POLYATOMIC ION BEAM DEPOSITION ON POLYMER SURFACES

In order to better understand the role of the chemistry and structure of polyatomic ions on surface modification and thin film growth, the deposition of mass selected polyatomic ion beams have been studied by several groups.[3,48,132,133] However, experimental studies can provide only limited and indirect information about surface reactions and film growth mechanisms. Complementary computer simulations[2-7,134-136] of polyatomic ion deposition provide valuable information about the details of polyatomic ion deposition. In computer simulation study, it is relatively easy to explore possible interaction mechanisms between reactant species and the surface under specific reaction conditions.[2,3,47] Computational simulations of polyatomic ion deposition on various substrates have been performed by several groups using molecular dynamics (MD) methods.[2,3,6,47,134,135,137,138] MD simulations are an ideal computational approach to study polyatomic ion bombardment because most of the important events in the deposition process occur within a few picoseconds. Therefore the simulations provide direct mechanistic information about the reactions.[45]

In previous work by Wijesundara *et al.*, the deposition of CH_3^+ and $C_3H_5^+$ on polystyrene (PS) surfaces at kinetic energies of 20-100 eV is considered in MD simulations and the results are compared to experimental findings for the analogous fluorocarbon ions CF_3^+ and $C_3F_5^+$ on PS.[2,3] In those studies, the ions were only deposited at angles normal to the PS surface. The experiments and simulations showed that the $C_3F_5^+/C_3H_5^+$ ions were more effective at growing films than the CF_3^+/CH_3^+ ions when

they were deposited at similar energies per atom (~6 eV/atom). Fragmentation of both types of ions increased when the ion energies were increased to 50 eV in both the experiments and simulations. The simulations provided insight into the dependence of the reaction products and penetration depths on the incident energies, ion structures, and the identity of the penetrating fragments.

In these studies, MD simulations of the deposition of a beam of polyatomic fluorocarbon ions onto PS surfaces are performed at experimental fluences to obtain insight into the mechanisms responsible for fluorocarbon thin film growth and the fluorination of the polymer. To facilitate these simulations, a new C-H-F many body empirical potential is developed based on Brenner's second-generation REBO potential for hydrocarbons.[116] The details of this potential are presented in chapter 2.

In addition, statistical studies for single $C_3H_5^+$ deposition are also performed to obtain more detailed information about the reaction between incident ion and polymer surfaces with respect to the effect of incident angle and structure of polymer. The effect of changing the deposition angle of atoms, ions and clusters on surface modification has been studied by many groups.[51,139-150] These studies find that metal ions are steered towards the top of existing islands by long-range attractive forces at angles greater than 50° and that the degree of surface roughness increases as the angle increases from the surface normal. They also show that the rapidity by which the ion is captured or is free to move within the surface changes with angle. When growth is considered for long times, increasing deposition angle has been linked to the formation of porous films that contain columnar structures. Finally, the degree of ion scattering from surfaces is found to increase as the angle increases.

The surface reactions that incident ions undergo are expected to be different on different surfaces. The chemical and physical properties of the surface are expected to affect the interaction between incident ions (or their fragments) and the surface. For example, PS and polyethylene (PE) have very different chemical and physical properties though they are composed of the same elements, carbon and hydrogen. PS has a higher glass transition temperature and melting temperature, and a stiffer structure than PE. These differences come from the presence of the bulky phenyl ring in the PS structure.[151] Figure 3-1 shows structure models of PS and PE chains.

3.1 Simulation Details

The MD simulations numerically integrate Newton's equations of motion with a third-order Nordsieck predictor corrector[124] using a timestep of 0.2 fs. Short-range interatomic forces are calculated using the new C-H-F potential for fluorocarbon deposition and Brenner's REBO potential for hydrocarbon deposition. Because of the

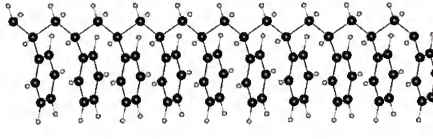

(a)

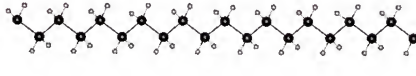

(b)

Figure 3-1. Models of (a) PS and (b) PE chains. Black sphere and gray spheres represent carbon and hydrogen atoms, respectively.

empirical, classical nature of these potentials, electronic effects such as electronic excitations or charging of the atoms is not included. Therefore ions with positive charges are treated as reactive radicals rather than true ions with an actual charge. It is recognized that the presence of a positive charge will influence the chemical reactions that occur during deposition. However, it is also true that many incident ions are rapidly neutralized as they approach the surface. The expectation is that the simulation results are qualitatively correct and can provide insight into the processes taking place during polyatomic ion deposition on polymer. Long-range van der Waals interactions are included in the form of a LJ potential[124] that is only active at distances greater than the covalent bond lengths.

3.1.1 Continuous Fluorocarbon Ion Deposition on PS Surface

The polymer surface used in the fluorocarbon ion deposition is syndiotactic crystalline polystyrene, which contains eight layers for a total thickness of 50 Å. The three bottom layers of the surface and atoms within 5-10 Å from the four sides of the slab have Langevin frictional and stochastic forces[124] applied to maintain the surface temperature at 300 K. The rest of the atoms in the system have no constraints and are designated as 'active'. Periodic boundary conditions[124] are also applied within the plane of the surface to mimic an infinite surface and effectively double the number of thermostat atoms at the edges of the surface. Figure 3-2 shows the initial PS surface schematically.

After the system is thoroughly equilibrated, a beam of 240 $C_3F_5^+$ (CF_2–C^+F–CF_2) ions or a beam of 400 CF_3^+ ions is deposited on the PS. Each ion in the continuous beam is deposited at randomly chosen locations within the active region of the surface at random orientations relative to the surface. The total kinetic energies of the ions are 50

eV and the incident angle is along the surface normal. In both cases the total fluence is equal to 1.8×10^{16} F atom/cm^2, which is the same as experimental values corresponding to ion currents of 80 nA.[3] In order to investigate the effect of incident energy, an additional 105 $C_3F_5^+$ depositions are performed at 100 eV/ion with the total fluence of 0.8×10^{16} F atom/cm^2. After the ion beam deposition process is complete, the systems are fully equilibrated for 25 ps.

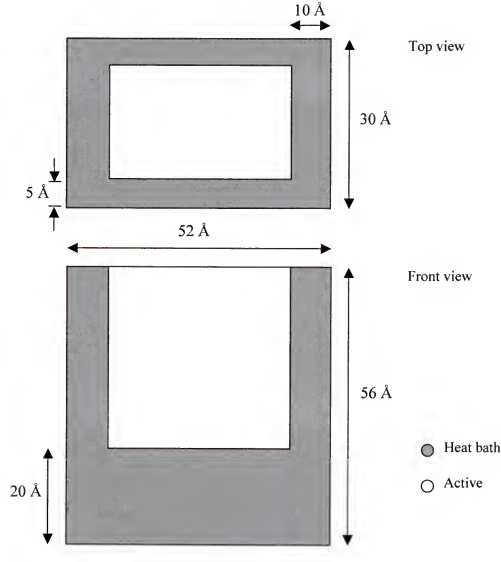

Figure 3-2. Schematic representation of initial PS substrate.

predicted to form on the time scales of these simulations. Rather, numerous fluorocarbon ions and dissociated ion fragments are embedded in the PS, some of which form covalent bonds to PS carbon atoms. The polymer backbone structures are randomized and, consequently, their volume increased by the ion bombardment. Due to their higher incident velocity, CF_3^+ ions induce more disordering and swelling than $C_3F_5^+$ ions.

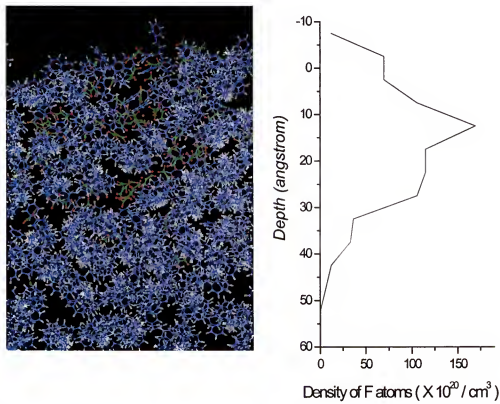

(a)

Figure 3-3. Structure models of PS surfaces (red spheres are F atoms, green spheres are C atoms from the ions, blue spheres are C atoms from the PS and white spheres are H atoms). (a) Snapshot of the PS surface after $C_3F_5^+$ ion beam deposition and equilibration and depth profile of F density in the PS surface. (b) Snapshot of the PS surface after CF_3^+ ion beam deposition equilibration and depth profile of F density in the PS. The vertical scales of the depth profile graphs are matched with the snapshots. The negative depth corresponds to swelling of the PS surfaces, as discussed in the text. Zero depth corresponds to the initial surface level of the pristine substrates.

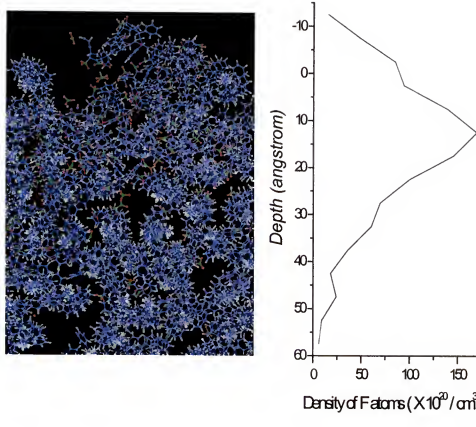

(b)

Figure 3-3. Continued.

Surface etching yields are approximately the same for the two ions at 0.26 C atom/ion and 0.29 H atom/ion for $C_3F_5^+$ and 0.28 C atom/ion and 0.31 H atom/ion for CF_3^+. However, total F uptake and deposition yield are higher for CF_3^+ than $C_3F_5^+$ at 4.29×10^{15} F atoms/cm^2 and 5.12×10^{15} atoms/cm^2 for $C_3F_5^+$ and CF_3^+, respectively. Deposition yields are 23.2% C and 23.5% F by $C_3F_5^+$, and 26.5 % C and 28.1% F by CF_3^+. This result can be attributed to the size difference between $C_3F_5^+$ and CF_3^+ as well as the difference in their incident velocities. In other words, more ions and ion fragments scatter away from the PS surface during $C_3F_5^+$ ion beam deposition because of the lager size and lower velocities of the ions compared to the CF_3^+ ion beam.

3.1.2 Hydrocarbon Ion Deposition on PS and PE surfaces

The PS surfaces contain eight layers for a total thickness of 50 Å. Langevin Equation of motion is applied to the atoms in the bottom layer of the surface and atoms within 2.5 Å from the four sides of the slab to maintain the surface temperature at 300 K.[124] Periodic boundary conditions are also applied within the plane of the surface. The PE surface contains ten layers and its total size is same with PS surface. The other configurations, such as thermostat and periodic boundary condition are also same with PS surface.

The simulations are performed with the ground state isomeric structure of $C_3H_5^+$ (CH_2–C^+H–CH_2). It was previously predicted that the ground state structure is most prevalent experimentally, despite the fact the ions have significant internal energy that could lead to excited isomeric structures.[3] The ions are deposited at various locations within the active region of the surface at several orientations relative to the surface. The total kinetic energies of the ions are 25 and 50 eV/ion, and the incident angle is normal to surface. In order to investigate the effect of incident angle on the surface reaction, additional $C_3H_5^+$ ion depositions are performed to the PS surface at the incident angles of 15°, 45°, and 75° from the surface normal. In these additional depositions, the total kinetic energies of the ions are fixed at 50 eV. Deposition at each condition is examined in 80 trajectories and the simulations run from 0.2 to 1.2 ps before it is determined that the system has reached an equilibrium state.

3.2 Results and Discussion

3.2.1 Continuous Fluorocarbon Ion Deposition on PS

Figure 3-3 shows the PS models after the deposition of the $C_3F_5^+$ and CF_3^+ ion beams and the subsequent equilibration. No distinct fluorocarbon film layers are

Figure 3-3 also shows the depth profiles of F density in the PS after ion deposition is complete. The cause of the apparent negative depth is the swelling of the PS surfaces (zero depth is the initial level of the pristine surfaces). The F atoms spread slightly more widely and deeply as a result of CF_3^+ ion beam deposition than $C_3F_5^+$ ion beam deposition because of the smaller size and higher velocity of the CF_3^+. However, the highest density of F occurs at a depth of 10-15 Å for both $C_3F_5^+$ and CF_3^+ ion beams. The average penetration depths of F and C atoms are also very similar. Specifically, the average penetration depths are 16.0 Å for both C and F atoms after $C_3F_5^+$ ion deposition, and 15.9 and 15.2 Å for C and F, respectively, in the case of CF_3^+ ion deposition. More F atoms chemically bond to the PS during CF_3^+ ion deposition than during $C_3F_5^+$ ion deposition, as shown in Tables 3-1 and 3-2. In general, ions or ion fragments that form covalent bonds with polymer substrate have smaller penetration depths than non-bonded, embedded species. This explains why the penetration depths of F atoms for CF_3^+ deposition are similar to the penetration depth for $C_3F_5^+$ deposition. Thus, with regard to the depth of surface modification, CF_3^+ deposition is approximately equivalent to $C_3F_5^+$ deposition under conditions of experimental fluence where the CF_3^+ ions have higher incident velocities than the $C_3F_5^+$ ions.

Despite these similarities in the overall results between $C_3F_5^+$ and CF_3^+ ion beam deposition processes, the simulations predict that the detailed fluorination mechanisms of the PS surface by the $C_3F_5^+$ and CF_3^+ ions are very different from one another, as shown in Tables 3-1 and 3-2. Intact C_3F_5 that is simply embedded within the substrate is the most abundant species in the PS surface deposited with $C_3F_5^+$ ion beam and corresponds to over 11% of incident $C_3F_5^+$. CF_2 is one of the most reactive ion fragments, as over

Table 3-1. Surface density of indicated species that remain bonded to carbon atoms in, or are embedded within, the PS surfaces after $C_3F_5^+$ deposition. "Embedded" means the species are simply embedded in the surface on the time scales of the simulations.

	Density ($\times 10^{13}$ cm^{-2})	
	Covalently bonded	Embedded
C_3F_5	6.1	44.1
C_3F_n (except C_3F_5)	3.0	3.0
C_2F_n	7.6	9.1
CF_2	10.6	9.1
CF	1.5	1.5
C_nF_m ($n > 3$, $m > 5$)	0	6.1
F	4.6	13.7

Table 3-2. Surface density of indicated species that remain bonded to carbon atoms in, or are embedded within, the PS surfaces after CF_3^+ deposition.

	Density ($\times 10^{13}$ cm^{-2})	
	Covalently bonded	Embedded
CF_4	0	7.6
CF_3	19.8	36.5
CF_2	38.0	24.3
CF	4.6	0
C_2F_n	4.6	10.6
F	109.4	13.7
F_2	0	1.5

50% of deposited CF_2 forms covalent bonds with PS chains. For CF_3^+ deposition, F bonded to a PS chain is the most frequently observed particle and corresponds to 6% of all incident F atoms. These F atoms are attached to the PS chains by replacing H atoms within the PS structure or capping the ends of broken chains. CF_2 is again found to be one of the major, reactive ion fragments.

There is some controversy about the role of CF_x (especially CF_2) in fluorocarbon film deposition on Si and SiO_2 surfaces from plasma. Spectroscopic analysis indicates that CF_2 fragments are major building blocks of fluorocarbon films[38,152] and some researchers correlate adsorbed CF_2 with gaseous phase CF_2.[152-154] This suggests that direct deposition of CF_2 plays a major role in fluorocarbon film growth. However, other researchers argue that there is no direct correlation between gaseous phase CF_2 and fluorocarbon film growth.[38,155,156] In these simulations, CF_2 fragments are found to be the second most abundant and reactive species produced, regardless of the type of ion in the beam. In the case of $C_3F_5^+$, over 50% of the deposited CF_2 fragments form covalent bonds with the PS chains while in the case of CF_3^+, 61% of the deposited CF_2 ions form covalent bonds with the PS chains. Furthermore, because CF_2 has two active sites, it can act as a cross-linking agent between neighboring PS chains. Some cross-links are predicted to form within the PS, as shown in Figure 3-4. Thus, these MD simulations indicate that when either $C_3F_5^+$ or CF_3^+ polyatomic ions are deposited on a surface, significant amounts of CF_2 ion fragments are generated that react with the surface. Although the substrates in these simulations are polymeric rather than Si or SiO_2, these results are consistent with reported spectroscopy results[2,3] and support the argument that fluorocarbon films are not formed exclusively by direct interaction of gaseous CF_2 with

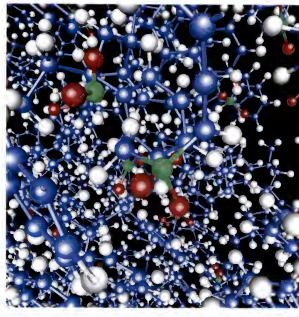

Figure 3-4. Snapshot form the MD simulations showing a CF_2 fragment linking two PS chains. The color schemes are the same as in Figure 3-3.

the surface. Rather, these simulations predict that CF_2 species are readily formed by the dissociation of polyatomic ions in surface collisions.

Tables 3-3 and 3-4 show the yields of the major scattering species for CF_3^+ and $C_3F_5^+$ ion beam deposition, respectively. In the case of the CF_3^+ ion deposition, CF_3, CF_2 and F are the major scattering species. The scattering data for CF_3^+ ion deposition agrees with reported experimental results[157-159] that show that relative amounts of CF_3, CF_2, CF and F depend on the incident energy of the ion, and more CF and less CF_3 emerge as scattering fragments at higher incident energy. While the simulations do predict that somewhat fewer CF scattering fragments are produced than experimental results at the same incident energy, this difference is attributed to the fact that a softer surface is considered in the simulations than in the experiments.

In the case of $C_3F_5^+$ deposition, C_3F_5, C_2F_3 and CF_2 are the major scattering

Table 3-3. Yield of scattering species for CF_3^+ deposition. (n>1, m>2)

Species	CF_3	CF_2	CF	F_2	F	C_nF_m
Yield (%)	33.0	23.5	2.0	2.0	10.8	4.8

Table 3-4. Yield of scattering species for $C_3F_5^+$ deposition.

Species	C_3F_5	C_3F_4	C_2F_3	C_2F_2	CF_2	CF	F
Yield (%)	32.5	3.8	14.6	7.5	20.8	5.8	8.8

species. Combined with the data shown in Table 4-3, this result indicates that most of the ion dissociation occurs by breaking one of the C-C bonds in the incident $C_3F_5^+$. Some experiments under similar conditions find that CF_3 is a major scattering fragment and no significant amount of CF_2 is detected, in disagreement with these predictions,[159] while others find that CF_2 is a major fragment and little CF_3 is detected, in good agreement with results predicted in these simulations.[3] In these simulations, the ground state of $C_3F_5^+$ (CF_2-C^+F-CF_2) is used. However, a higher energy state isomer, such as CF_3-C^+=CF_2 or CF_3-CF-C^+F is possible, and these have CF_3 moieties. In a previous study, the effect of different structures of $C_3H_5^+$ on the results of deposition on PS was explored, and found that if the incident ion contains CH_3 moieties, CH_3 fragment are preferentially produced as major species by dissociation.[3]

In Figure 3-5, the F atom uptake and total deposition yield are presented. For $C_3F_5^+$ deposition, the amount of F uptake increases continuously though the deposition yields decrease at high fluence, converging to 29% at the later stage of deposition. This implies that the fluorocarbon film will be continuously built up as the process progresses. Equilibrium conditions are reached when the deposition rate is equal to the etching rate.

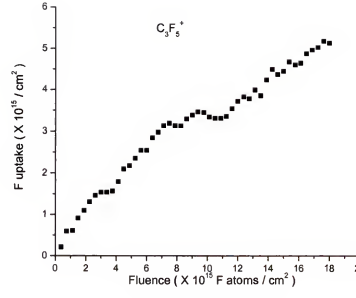

(a)

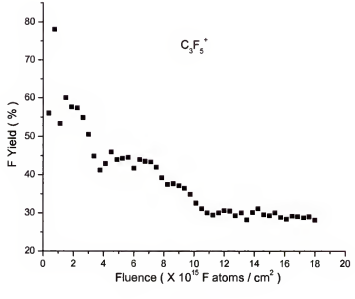

(b)

Figure 3-5. F uptake and total deposition yield of F as function of fluence during deposition. a) F uptake for $C_3F_5^+$ deposition. b) Deposition yield of F for $C_3F_5^+$ deposition, c) F uptake for CF_3^+ deposition, d) Deposition yield of F for CF_3^+ deposition

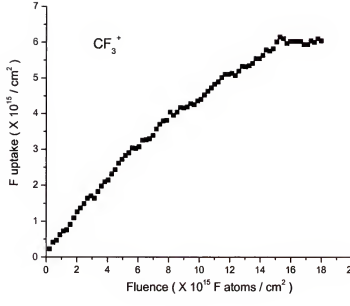

(c)

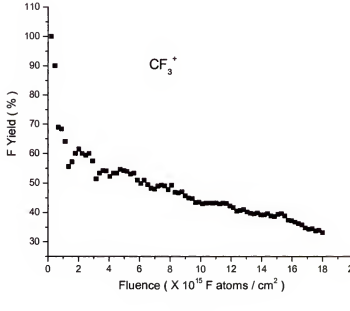

(d)

Figure 3-5. Continued.

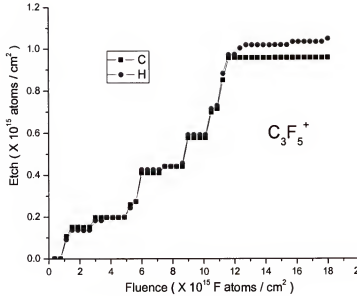

(a)

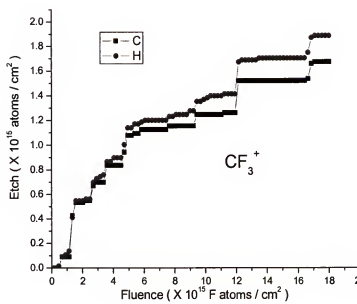

(b)

Figure 3-6. Degree of PS surface etching during ion beam deposition.

It has been reported that fluorocarbon films are maintained at constant levels from a certain stage of the deposition process onwards when the fluorocarbon ion beams are deposited on Si surfaces at 100 eV.[47] Unlike the high energy ion deposition on hard surfaces such as Si, it is more likely that unlimited film growth occurs on relatively soft polymer surfaces by low energy ion deposition. At the stage where the deposition yield starts to converge to a constant value, the surface etching also decreases, as shown in Figure 3-6(a) for the $C_3F_5^+$ deposition processes. Therefore, it appears that this system is approaching a steady-state, continuous film growth stage after an induction period.

For CF_3^+ deposition, Figure 3-5 shows that the deposition yield decreases continuously to the final deposition stage without any sign of leveling off. Additionally, it appears that the amount of F uptake tends to converge to a constant value at the latter stages of the deposition process. However, the final deposition yield of CF_3^+ is still large, and the plateau in Figure 3-5(c) might be temporary because such a plateau is also briefly seen in Figure 3-5(a). Figure 3-6(b) shows that the etching process is still developing at the final stage of deposition though the rate keeps decreasing. Therefore the CF_3^+ deposition process does not reach steady-state on the time scale of these simulations.

It should be pointed out that the final values of F uptake in Figure 3-5 are higher than the total fluorine density summed from Tables 3-1 or 3-2 because the values presented earlier are obtained after long equilibration processes. During equilibration, more than 15% of the deposited F atoms are desorbed from both PS surfaces treated with $C_3F_5^+$ and CF_3^+. Most of the desorbed F atoms were simply embedded in the surface before equilibration and were thus not covalently bonded to the PS surface.

Figure 3-7 shows the average penetration depths for the major species on the PS

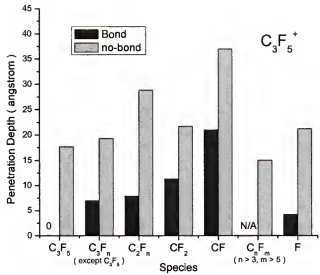

(a)

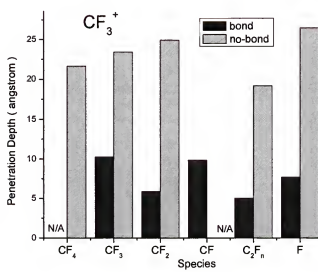

(b)

Figure 3-7. Average penetration depths of indicated species in the PS surfaces. "Bond" means that the species form covalent bonds with C atoms in the PS chains and "no-bond" means the species are simply embedded in the surface on the time scales of the simulations. a) $C_3F_5^+$ deposition, b) CF_3^+ deposition

surfaces. Zero penetration depth of bonded C_3F_5 means that those particles stay right on the surface. As mentioned previously, a variety of ions and ion fragments that form covalent bond to PS chains show much smaller penetration depths than the same species that is simply embedded in the substrate. Therefore, three dominant species in CF_3^+ deposition, F, CF_2, and CF_3, that bond to PS chains have penetrations depths that are equal to or less than 10 Å. Thus, these species are very effective at fluorinating the PS surface. For $C_3F_5^+$ ion deposition, the dominant species that are bonded to PS chains, CF_2, C_2F_n and C_3F_5, show penetration depths of 11, 8, and 0 Å, which also makes them effective fluorinators of the PS surface. Alternatively, C_2F_n and C_3F_5 can be thought of as more effective precursors for fluorocarbon polymer film growth than smaller fragments because they contain more than one carbon atoms and may have more than one active site. These larger fragments can more readily react and connect with other fluorocarbon

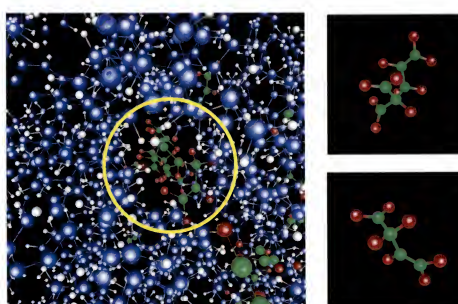

Figure 3-8. A portion of the PS structure after deposition of 240 $C_3F_5^+$ ions. a) Precursors of fluorocarbon polymer within the PS. b) and c) show some precursors on their own for clarity. The color schemes are the same as in Figure 3-3.

ions or fragments to grow polymer-like structures than smaller fragments, as shown in Figure 3-8. As a point of comparison, F atoms, the most dominant species in CF_3^+ deposition, deactivates an active site in the PS once it forms a chemical bond. Thus, these simulations predict that CF_3^+ deposition is more effective than $C_3F_5^+$ deposition in short-term treatments at fluorinating PS surfaces but $C_3F_5^+$ deposition is more effective at growing fluorocarbon polymer layers.

In order to investigate the effect of incident energy on the surface reaction and film growth, 105 $C_3F_5^+$ depositions at 100 eV/ion are performed as well. For proper comparison, PS surface that is equilibrated after 105 $C_3F_5^+$ depositions at 50 eV/ion is also prepared. Figure 3-9 shows the part of PS surfaces from the simulations after $C_3F_5^+$ ion beam deposition at 100 eV and 50 eV with the total fluence of 0.8×10^{16} F atom/cm^2. Due to the higher ion velocity, ion deposition with 100 eV of kinetic energy induces more

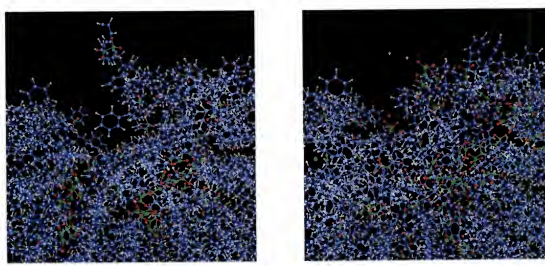

(a) (b)

Figure 3-9. Structure models of part of the PS surfaces (color scheme is same with Figure 3-3). a) Snapshot of the PS surface after 105 $C_3F_5^+$ deposition at 100 eV/ion. b) Snapshot of the PS surface after 105 $C_3F_5^+$ deposition at 50 eV/ion.

disordering of the PS than ion deposition at 50 eV. In addition, significantly more etching of the PS surface occurs at 100 eV/ion. Surface etching yields are 1.10 C atom/ion and 1.30 H atom/ion at 100 eV, and 0.28 C atom/ion and 0.28 H atom/ion at 50 eV. Although ion bombardment at 100 eV induces more surface damage, the total F uptake and deposition yield are higher at 100 eV than at 50 eV. For instance, F uptakes are 4.61×10^{15} F atoms/cm^2 and 2.72×10^{15} atoms/cm^2 for deposition at 100 eV and 50 eV, respectively. Deposition yields of F atom are 57.7 % and 34.1 % for deposition at 100 eV and 50 eV,

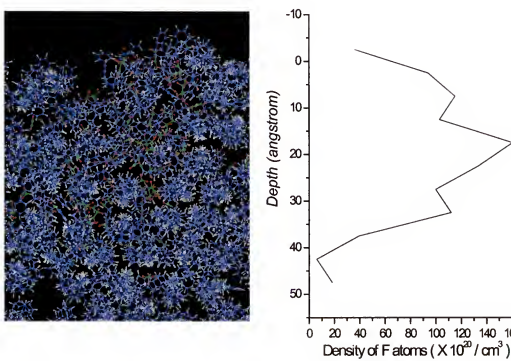

(a)

Figure 3-10. Structure models of PS surfaces. a) Snapshot of the PS surface after 105 $C_3F_5^+$ deposition at 100 eV/ion and a depth profile of F density in the PS surface. b) Snapshot of the PS surface after deposition at 50 eV/ion and depth profile of F density in the PS. The vertical scales of the depth profile graphs are matched to the snapshots. The negative depth corresponds to swelling of the PS surfaces, as discussed in the text. Zero depth is initial surface level of the pristine surfaces.

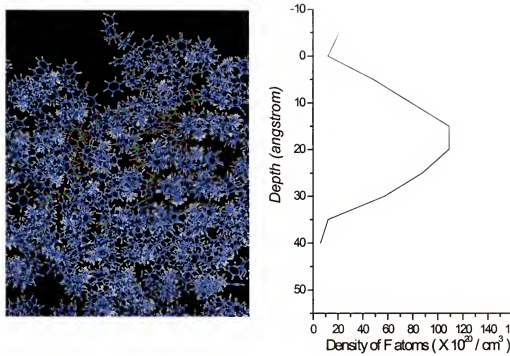

(b)

Figure 3-10. continued.

respectively. More incident ions are simply scattered away from the PS surface during deposition at 50 eV/ion.

Figure 3-10 shows almost the whole PS surface and depth profiles of F densities after 105 $C_3F_5^+$ deposition. The F atoms spread more widely and deeply at 100 eV deposition. The average penetration depths are 19.2 Å for C and 18.6 Å for F atoms after deposition at 100 eV/ion, and 17.3 and 17.2 Å for C and F, respectively, in the case of deposition at 50 eV/ion. The highest density of F occurs at a depth of 15-20 Å for both 100 eV/ion and 50 eV/ion deposition processes.

Table 3-5 and 3-6 show the surface density of the indicated species formed from the incident $C_3F_5^+$ ions that remain at the PS surfaces after 105 $C_3F_5^+$ deposition

Table 3-5. Surface density of indicated species that remain bonded to carbon atoms in, or are embedded within, the PS surfaces after 105 $C_3F_5^+$ deposition at 100 eV/ion.

	Density ($\times 10^{13}$ cm^{-2})	
	Covalently bonded	Embedded
C_3F_5	0	6.1
C_3F_n (except C_3F_5)	1.5	6.1
C_2F_2	0	28.9
C_2F_n (except C_3F_5)	12.2	18.2
CF_2	21.8	19.8
CF_n	7.6	13.7
C_nF_m ($n > 3$, $m > 5$)	9.1	1.5
F	56.2	12.2

Table 3-6. Surface density of indicated species that remain bonded to carbon atoms in, or are embedded within, the PS surfaces after 105 $C_3F_5^+$ deposition at 50 eV /ion.

	Density ($\times 10^{13}$ cm^{-2})	
	Covalently bonded	Embedded
C_3F_5	1.5	28.9
C_3F_n (except C_3F_5)	0	3.0
C_2F_n	4.6	9.1
CF_2	4.6	10.6
CF	3.0	1.5
C_nF_m ($n > 3$, $m > 5$)	1.5	1.5
F	1.5	12.2

at 100 eV and 50 eV, respectively. A more diverse sampling of ion fragments are formed at 100 eV, and more of these fragments form covalent bonds to the PS, than is the case for deposition at 50 eV. This is highlighted by the fact that at 100 eV, very few intact C_3F_5 groups survive deposition but are the most abundant species formed at 50 eV. Despite this increased dissociation of the incident ions at 100 eV, a significant number of large species that consist of more than three carbon atoms is observed at this energy. These large species are important precursors of fluorocarbon polymer film.

In addition, large amounts of fluorine atoms that covalently bonded with carbon atoms of PS chains are found in 100 eV deposition and most of these F atoms replace hydrogen atoms in PS chains. However, only a few fluorine atoms are observed in 50 eV deposition. Therefore, $C_3F_5^+$ beam deposition at 100 eV is more efficient for fluorination of PS substrate than 50 eV deposition. However, surface damage is more severe in 100 eV deposition.

3.2.2 Angular Influence of $C_3H_5^+$ Ion Deposition on PS Surface

The simulations are performed with the ground state structure of $C_3H_5^+$ (CH_2–C^+H–CH_2). It was previously predicted that the ground state structure is most prevalent experimentally despite the fact the ions have significant internal energy that could lead to excited state structures.[2,3] The etching effects are predicted to be negligible even though hydrogen atoms are knocked loose from the surface at all the angles considered. Instead, the ions deposit intact, fragment, or scatter from the PS surface. The averaged results for all the angles considered are summarized in Table 3-7.

The Table 3-7 shows that the number of ions that scatter from the surface increases as the angle increases from the surface normal, in agreement with findings in the literature for other systems.[147] At 75° ions are scattered away in 56% of the trajectories

Table 3-7. Percentage of occurrence of the indicated events averaged over 80 trajectories at different incident angles.

	0°	15°	45°	75°
Simple scattering from the surface	2.2	7.5	11.3	51.3
Scattering from the surface with a captured surface atom(s)		1.3	2.5	5.0
Embedding within the surface	22.5	23.8	15.0	
Incorporation with the surface	15.7	23.8	26.3	13.8
Dissociation (Loosing one or more H atoms)	27.9	13.8	15.0	13.8
Dissociation $CH_2 + C_2H_3$	23.6	21.3	21.3	11.3
Dissociation $CH_3 + C_2H_2$	1.1	1.3		
Dissociation $CH_2 + C_2H_2 + H$	4.5	3.8	1.3	2.5
Dissociation $CH + C_2H_3 + H$	3.4	1.3	1.3	1.3
Dissociation $CH + C_2H_2 + H + H$			1.3	
Dissociation $CH_2 + C_2H + H + H$			1.3	
Dissociation $CH_2 + CH_2 + CH$		2.5	1.3	1.3
Dissociation $CH_2 + CH + CH + H$			1.3	

without any dissociation. In contrast, ions scatter from the surface in only 2% of the trajectories at normal incidence. Overall, at smaller angles (closer to the surface normal), ions are more likely to dissociate. At normal incidence, the ions dissociate in 61% of the trajectories, whereas they dissociate in only 30% of the trajectories at 75°. At all angles, $CH_2 + C_2H_3$ is the most common dissociation reaction. At 15°, the ions deposit intact in 48% of the trajectories, the largest percentage of any of the angles considered, while the ions deposit intact in 38% and 41% of the trajectories at 0° and 45°, respectively. The ion fragments indicated in Table 3-7 react with the surface atoms after dissociation in most cases. Therefore, the exact structures of fragments may be different from the structures shown in the table after equilibration. At normal incidence, more trajectories result in the scattering of hydrogen atom(s) from the polyatomic ions or the PS than is the case at

larger angles. This indicates that the kinetic energy of the ions is transferred more efficiently to breaking bonds at normal incidence. Similarly, more carbon-carbon bonds in the ions are broken at normal incidents.

Figure 3-11 summarizes the number of ion fragments that are bonded to, or embedded in, the PS surface 0.8-1.2 ps after deposition. The embedded fragments penetrate the PS surface but do not form bonds with the PS carbon atoms on the time scales of these simulations. 'C' and 'H' represent carbon and hydrogen from the polyatomic ion while 'h' is hydrogen from the PS surface. On the whole, the smallest amount of deposition occurs at 75°. From Figures 3-11 (a)-(c) it is clear that incident angle does not greatly affect the total number of C_3H_y species that remain on the PS surface up to 45°. Slightly more C_3H_5 is deposited at 15° and 45° than 0° because of the greater amount of dissociation that occurs at normal incidence. However, slightly more C_3H_n is deposited at 0° and slightly more $C_3H_nh_m$ is deposited at 15°. At 75°, the amount of scattering is so large that significantly fewer large fragments are deposited on or embedded in the surface. These trends are also true for C_2H_y fragments, as indicated in Figures 3-11 (d)-(e). Slightly more C_2H_n and $C_2H_nh_m$ result at 0° but the second greatest amount varies between 45° and 15°. More hydrocarbon fragments that contain only one carbon atom (especially CH_2) remain on the PS surface after deposition at 15° and 45° than 0°, as indicated in Figures 3-11 (f)-(h). Slightly more CH_2 and CH_n is deposited 45° while slightly more CH_nh_m results at 0°. The majority of the CH_2 fragments form one or two bonds with carbon atoms from the PS backbones (see Figure 3-12). This indicates that CH_2 fragments play a major role in the cross-linking of PS surface. At 0° many CH_y fragments bond to hydrogen atoms that were originally bonded to PS carbon atoms. At

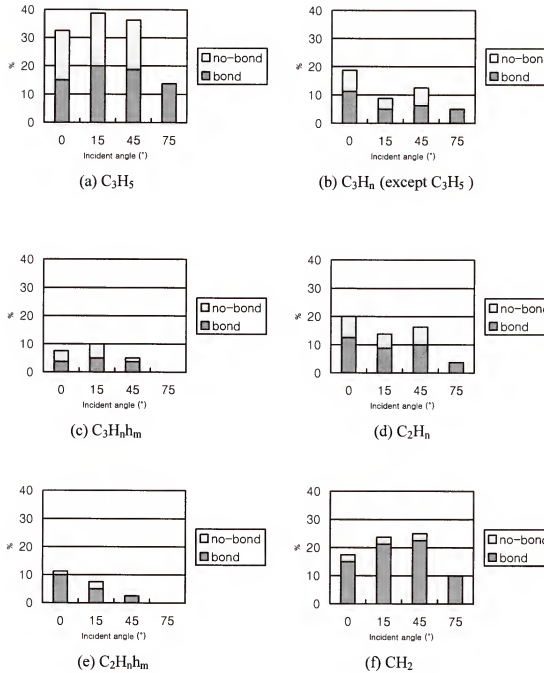

Figure 3-11. Percentages of the indicated product species that remain bonded to carbon atoms in the PS surface or are embedded in the PS surface. The results represent the averaged data from 80 trajectories. 'Bond' means that the indicated species formed bonded with carbon atoms in the PS.

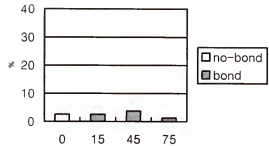

(g) CH_n (except CH_2)

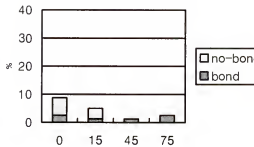

(h) CH_nh_m

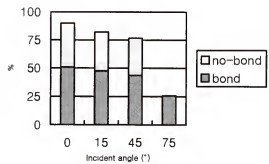

(i) Total carbons

Figure 3-11. continued

75°, only a few trajectories result in the dissociation of the polyatomic ions, so not many fragments are formed. These results are consistent with the finding that CF_y (especially CF_2) ions or radicals generated in fluorocarbon plasmas are considered to be the dominant precursors to polymer film formation.[14,152-154] Consequently, if the reactivity and behavior of polyatomic hydrocarbon and fluorocarbon fragments in plasma are similar to each other, these results indicate that polymer surface modification in fluorocarbon plasma or by ion beam deposition may be more efficient at small incident angles.

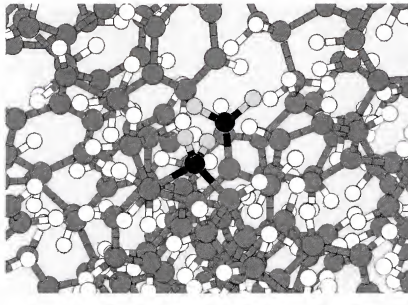

Figure 3-12. Snapshot from the MD simulations showing the products of the dissociation of the $C_3H_5^+$ ion into CH_2 fragments that bond to the PS surface. (Black spheres are carbon atoms from ion, dark gray spheres are carbon atoms from PS, light gray spheres are hydrogen atoms from the ion, and white spheres are hydrogen atoms from PS).

The number of carbon-carbon and carbon-hydrogen PS bonds that are broken as a result of the deposition of the ions decreases as the deposition angle increases, as shown in Figure 3-13. The largest decrease occurs at 75°, while an average of 0.9-1 bonds are broken for 0°, 15° and 45°. Bond breaking within the PS leads to cross-linking with the ions or fragments, as discussed above and shown in Figure 3-12, but can also lead to cross-linking between polymer backbones.[160] Thus, small angles can lead to appreciable cross-linking despite the fact that not all of the ion's kinetic energy is directed into the surface.

Figure 3-11 (i) summarizes the total amount of carbon deposited on the PS surface during the 80 trajectories per angle. While ion bombardment at normal incidence deposits the greatest amount of carbon, ion bombardment at 15° and 45° results in only slightly

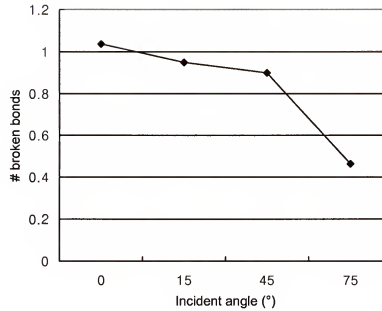

Figure 3-13. Average number of broken bonds per trajectory in the PS surface as a result of $C_3H_5^+$ deposition at the indicated angles over the 80 trajectories.

less carbon deposited on the surface. However, bombardment at 75° results in significantly less (about ¼ the amount at 0°) carbon deposited on the surface.

Figure 3-14 shows the average penetration depth for the ions or significant ion fragments as a function of deposition angle. The Figure indicates that more fragments that contain carbon atoms remain near the surface at 45° (ions penetrate the PS 3.5-5.5 Å) compared to normal incident angles (ions penetrate the PS 6.2-7.2 Å) or 15° (ions penetrate the PS 6.0-7.0 Å). Therefore, these simulations predict that a medium inclined angle is best for thin-film deposition close to the surface. Although the penetration depth for ions and major fragments are very small at 75°, too large an angle results primarily in scattering and the number of ions or major fragments considered in Figure 3-14 for 75° is small (as indicated in Table 3-7 and Figure 3-11).

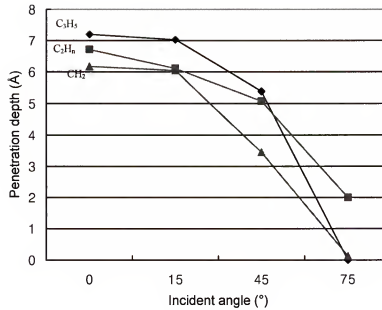

Figure 3-14. Average penetration depths of major species (C_3H_5, C_2H_n, CH_2) from the incident ions as a function of angle. Zero penetration depth means that the indicated species is adsorbed right on the surface.

Larger penetration depths lead to a larger number of bonds broken in the PS surface, so the data contained in Figures 3-13 and 3-14 are correlated. However, Figure 3-11 shows that there is little difference in the number of carbon atoms bonded with PS carbon atoms at 0°, 15°, and 45° on the time scales of the simulations. Instead, about half of the carbon atoms merely embed within the PS surface without forming covalent bonds to the PS backbone chains surface. It is likely that the embedded fragments would form bonds with the PS chains or react with succeeding incident ions if continuous bombardment simulations had been performed or if the trajectories ran for longer times.

3.2.3 Polystyrene vs. Polyethylene

Table 3-8 summarizes the results obtained from the MD simulations for PS and PE surfaces at ion energies of 50 and 25 eV. The ion fragments indicated in the table react

with the surface atoms after dissociation in most cases. Therefore, the exact structures of the fragments may be different from the structures shown in the table after equilibration has occurred. No carbon atoms are removed from the polymer surfaces. However, some hydrogen atoms are detached from the polymer chains and knocked loose from the surface. Therefore, etching effects are predicted to be negligible in all the cases considered.

Ions dissociate on the PS surface in many more trajectories than on the PE surface at 50 eV. On the PS surfaces, dissociations of incident ions occur in 61% of the trajectories, whereas they dissociate in 40% of the trajectories on the PE surfaces. On both PS and PE surfaces, the loss of hydrogen atom(s) and the $C_2H_5 \rightarrow CH_2 + C_2H_3$ dissociation reaction are the most common chemical reactions. At 25 eV, only a few ions dissociate on the PS surfaces and the ions deposit intact in 70% of the trajectories. No ion dissociates on the PE surfaces at 25 eV and the ions remain on the surface in only 10%

Table 3-8. Percentage of occurrence of the indicated events in the MD simulations of $C_3H_5^+$ deposition averaged over 80 trajectories.

	PS		PE	
	50 eV	25 eV	50 eV	25 eV
Simple scattering from the surface	2.2	27.5	7.5	77.5
Scattering from the surface with a captured surface hydrogen			3.8	12.5
Embedding within the surface	22.5	51.3	6.3	3.8
Incorporation with the surface	15.7	18.8	42.5	6.3
Dissociation (Loosing one or more H atoms)	27.9	1.3	13.8	
Dissociation $CH_2 + C_2H_3$	23.6	1.3	17.5	
Dissociation $CH_3 + C_2H_2$	1.1		3.8	
Dissociation $CH_2 + C_2H_2 + H$	4.5		3.8	
Dissociation $CH + C_2H_3 + H$	3.4			
Dissociation $CH + CH_2 + CH_2$			1.3	

trajectories. As mentioned above, reactive fragments of ions or radicals generated in fluorocarbon plasma, such as CF_2, are considered to be important precursors to polymer film formation.[14,152-154] Therefore, it can be inferred that ion energies of 25 eV are a poor choice for thin film formation on PS because most of the incident ions remain intact.

The PS is stiffer than the PE because molecular motions are hindered by the bulky phenyl rings. When the incident ions hit the PS chains, the impact energy cannot be absorbed through deformation of the chains as efficiently as is the case in PE. Therefore, the impact energy is concentrated on a smaller part of the PS chains and leads to the dissociation of the incident ions more easily than on PE. This result agrees with the findings of other reports in the literature.[118,161,162]

Ions scatter from the surface in many more trajectories on the PE surface than on the PS surface. At 25 eV, the ions are scattered away in 90% of the trajectories on the PE surface, whereas ions scatter from the PS surface in only 28% of the trajectories. As mentioned above, the PE chains can accommodate the impact energy by deformation through several chain segments. The excess energy can then be dissipated through the whole surface in the form of heat, which is removed through the Langevin frictional forces in the heat bath atoms. The energy can also be dissipated by restoring deformed chains to their original conformation that causes the incident ions to scatter from the surface. This mechanism is not favorable for PS due to the lack of chain mobility. At 50 eV, ions scatter from the surfaces in only 2% of the trajectories on PS and 11% of the trajectories on PE. Some ions abstract hydrogen atoms from the surface as they scatter away, especially on the PE surface. On the PS surface, if the incident ions detach

hydrogen atoms from the surface carbon atoms, they do not escape from the surface without dissociation.

Figure 3-15 summarizes the number of ion fragments that are bonded to, or embedded in, the PS and PE surface at 50 and 25 eV 0.8-1.2 ps after deposition. The embedded fragments penetrate the polymer surfaces but do not form covalent bond with the carbon atoms of the polymers on the time scale of these simulations. 'C' and 'H' represent carbon and hydrogen from the incident ion while 'h' is hydrogen from the polymer surfaces.[3,4] Overall, more fragments remain on the PS surface than on the PE surface. The exception is C_3H_5 ions, more of which remain on the PE surface than the PS surface at 50 eV. This is because more incident ions dissociate on the PS surface than on the PE surface (see Figure 3-15(a)). Figure 3-15(b) shows that many more C_3H_n fragments, generated from incident ions that lose one or some hydrogen atoms, are deposited on the PS surface than on the PE surface. At 25 eV, there is no ion fragmentation on the PE surface and only a few incident ions remain intact. This is because most of the ions scatter from the surface without dissociation. In contrast, 70% of incident ions remain on the PS surface, but the majority of them are merely embedded in the surface because 25 eV is not enough energy for the formation of new bonds with the surface atoms on the time scales of these simulations. For the major fragments, C_2H_n and CH_2, similar amounts are deposited on both surfaces as shown in Figures 3-15 (d) and (f). Slightly more C_2H_n stay on the PS surface, but the amount of CH_2 is almost the same on both surfaces. Excluding CH_2, only a small number of fragments that contain one carbon atom remain on either surface at 50 eV (Figure 3-15(g)).

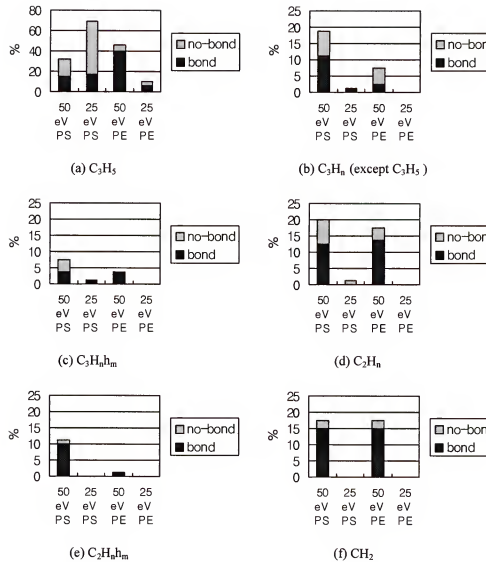

Figure 3-15. Percentages of the indicated product species that remain bonded to carbon atoms in, or are embedded within, the PS and PE surfaces at 50 and 25 eV. The results represent the averaged data from 80 MD simulation trajectories. 'Bond' means that the indicated species formed bonds with carbon atoms in the polymer substrates on the time scales of the simulations. 'No-bond' means that the indicated species were embedded in the polymer substrate but did not form covalent bonds with carbon atoms in the polymer on the time scales of the simulations.

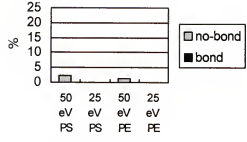

(g) CH_n (except CH_2)

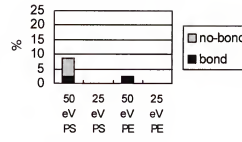

(h) CH_nh_m

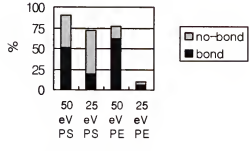

(i) Total carbons

Figure 3-15. Continued

The fragments that recombine with surface hydrogen atoms, $C_3H_nh_m$, $C_2H_nh_m$ and CH_nh_m, are more readily found on the PS surface than the PE surface (Figures 3-15 (c), (e) and (h)). This means that more hydrogen atoms are abstracted from polymer chains on the PS surface than on the PE surface. Figure 3-16 shows the average number of carbon-hydrogen and carbon-carbon bonds that are broken in the polymer as a result of the ion deposition. The number of broken bonds is almost the same for both polymers. As mentioned earlier, PE is more effective at dissipating the energy of impact than PS due to the increased flexibility of its chains. One might therefore infer that bonds in the PS surface may be broken more easily than bonds in the PE surface. However, 67% of carbon-carbon bonds in the PS surface are in phenyl rings. The energy needed to break

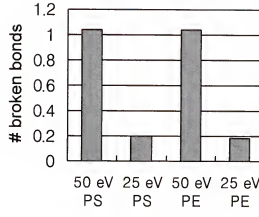

Figure 3-16. Average number of broken bonds in the PS and PE surfaces per MD trajectory as a result of $C_3H_5^+$ deposition at 50 and 25 eV. The results are averaged over 80 trajectories.

carbon-carbon bonds in the phenyl rings is greater than that needed to break single carbon-carbon bonds, such as are found in the PE surface. Specifically, the calculated bond energy of a single carbon-carbon bond is 3.69 eV while the calculated bond energy of a conjugated double carbon-carbon bond is 5.36 eV according to the reactive empirical bond-order potential used in the simulations.[116] Therefore, the probability of carbon-carbon bond dissociation in the PS is lower than that in the PE if the same energy is applied per carbon-carbon bond. This property compensates for the effectiveness of the PE in absorbing the impact energy, and makes the numbers of broken bonds almost the same for both polymers. The partial saturation of the phenyl rings on the PS occurs infrequently in the simulations. The vast majority of the interactions of the ions or ion fragments with the phenyl rings result in broken rings or the substitution of the ion or fragment for the phenyl hydrogen atoms. This is consistent with known aromatic chemistry[54] that shows that partially saturated phenyl rings are unstable and usually go

back to a resonance structure spontaneously by removing a hydrogen atom or substituent species.

The number of carbon-hydrogen bonds broken should be larger in PS than PE because the probability of carbon-carbon bond dissociation in PS is less for the same total number of broken bonds. This explains why more hydrogen atoms are detached from the PS surface than the PE surface.

Figure 3-15 (i) summarizes the total amount of carbon deposited on the PS and PE surfaces averaged over the 80 trajectories at 50 and 25 eV. The amount of carbon deposited on the PS surface is larger than on the PE surface, but the number of carbon atoms form the incident ions forming bonds with surface carbon atoms is larger on the PE surface at energies of 50 eV. When one carbon-carbon bond is broken, two reactive sites are formed in the polymer chain, whereas only one reactive site is made after breaking one carbon-hydrogen bond. Since carbon-carbon bond dissociation is more favorable on PE than PS, incident ions or fragments can form bonds with surface carbon atoms more easily on the PE surface. At 25 eV, most of the carbon deposited on the PS surface is in the form of intact incident ions, and only a small amount of carbon remains on the PE surface because most of the incident ions are scattered away.

Figure 3-17 shows the average penetration depth for the ions or significant ion fragments in PS and PE at 50 and 25 eV. The figure indicates that all three species penetrate more deeply into the PE surface than the PS surface at 50 eV. PE has better chain mobility than PS so that ions or fragments can squeeze into the PE substrate more easily. At 25 eV, the average penetration depth of the ions is smaller in PE than PS. However, the number of ions remaining on the PE surface is very small (10%) compared

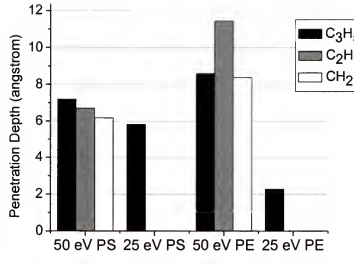

Figure 3-17. Average penetration depths of major species (C_3H_5, C_2H_n, CH_2) from the incident ions.

with the number of ions on the PS surface (70 %). Therefore, the number of ions near the surface cannot be larger in PE than in PS.

3.3 Conclusions

3.3.1 Continuous Fluorocarbon Ion Deposition on PS

For CF_3^+ deposition, F atoms play the most important role in fluorinating the PS surface, as the majority of them are covalently attached to the PS chains through replacement of native H atoms or capping the end of broken chains. CF_2 fragments are also an important long-lived species. In contrast, F atoms are a minor bi-product and CF_2 fragments are the most dominant species for $C_3F_5^+$ deposition on PS. The simulations thus predict that CF_3^+ deposition is more effective than $C_3F_5^+$ deposition for polymer fluorination because of the large amount of bare F atoms that are produced, while $C_3F_5^+$ deposition is more effective at producing precursors for fluorocarbon thin film growth

because of the larger structural size of the major ion fragments. Compared with real plasma or ion deposition processes, this simulation study only explores the very early stages of surface chemical modification and thin film growth but the results indicate likely atomic scale mechanisms responsible for these processes.

3.3.2 Angular Influence of $C_3H_5^+$ Ion Deposition on PS Surface

Overall, normal incident angles lead to the most reactive collisions. In 98% of the trajectories, the $C_3H_5^+$ ions or their fragments remain on the PS surface. In contrast, 56% of incident ions are scattered away from the PS surfaces without dissociation at 75°. The total amount of deposited carbon that remains at the surface is largest at normal incident angles. However, more ions or fragments remain near the surface at 45°. In addition, the amount of CH_2 fragments that remain at the surface is largest at 45° with the majority of these fragments bonded to the carbon backbones of the PS. Therefore, the simulations predict that the largest amount of CH_2 fragments, hydrocarbon analogues of CF_2, are deposited near the surface at 45°. Conclusively, deposition at an inclined angle such as 45° should be more efficient for shallow surface modification than normal incidence even though more scattering takes place.

3.3.3 Polystyrene vs. Polyethylene

It is predicted that the $C_3H_5^+$ ion deposition process to produce precursors for thin-film growth is more effective on the PS surface than on the PE surface, and deposition at 50 eV is more effective than deposition at 25 eV. More ions dissociate and remain on the PS surface, and more ions and fragments remain in a shallow region of the PS surface. In particular, at 25 eV the ion deposition process on the PE surface is very inefficient because 90% of the incident ions scatter from the surface. However, the amount of total

carbon deposited on the PE surface is not much smaller than the amount deposited on the PS surface. The amount of major fragments (C_2H_n and CH_2) deposited on both surfaces at 50 eV is almost the same.

A minor property of the PE substrate expected from these simulation studies is that relatively more carbon-carbon bonds are broken by ion deposition on the PE surface than on the PS surface. This bond breaking can affect the mechanical strength of the substrate. However, it can also lead to the formation of reactive sites to which incident ions or ion fragments can attach.

Thus, the simulations illustrate the atomic-scale mechanisms responsible for the differing surface modification effects of $C_3H_5^+$ deposition on crystalline PS and PE surfaces. These mechanisms would be expected to be found in mass-selected ion-beam deposition of polymer surfaces and in surface modification in plasma.

CHAPTER 4
CARBON NANOTUBE WELDING UNDER ELECTRON BEAM IRRADIATION

Compared with other techniques for forming nanotube junctions, electron beam irradiation has several advantages. For instance, there is less opportunity for contamination of the sample, and highly focused sub-nanometer scale beam spots are attainable. In addition, it can be performed with commercial electron microscopes. In this study classical MD[124] simulations are performed to produce crossed junction of CNTs under an electron beam that is above the irradiation threshold. The main goal of this study is to provide detailed structural characterization and thermal stability analysis of CNT junctions obtained under highly non-equilibrium processing conditions. The mechanical and electronic properties of the computationally synthesized junctions are also characterized and compared with those of comparable hand-built "ideal" junctions. Calculation of electronic structure was done by Dr. Fabrizio Cleri.

4.1 Simulation Details

To analyze a wide range of carbon structures over relatively long time scales, the interatomic forces in the systems are calculated using the many-body, reactive empirical bond-order (REBO) potential. It does not, however, allow for electronic excitations. These simulations therefore implicitly assume that the chemical reactions of the radicals created by electron irradiation are not fundamentally different from the chemical reactions of ionized atoms. It is noted, however, that even electronic structure based calculations including *ab-initio*, generally describe only ground electronic state and also do not capture dynamically ionization or electronic excitations.

The simulation setup (see Figure 4-1) is similar to that used in recent MD simulations of ion irradiation induced junction formation.[109] The initial configuration consists of two nanotubes crossed 90° with respect to each other. The regions at tube ends are fixed, i.e., the atomic motion at the ends are completely suppressed. In the rest of the system the atoms move according to the Newton's equation of motion, except that in the thermostat regions adjacent to the fixed regions, additional stochastic and dissipative forces are applied to atoms providing a Langevin thermostat that allows for the dissipation of the energy associated with the collision events. A combination of the noise and damping terms used in the thermostat regions is selected that corresponds to a temperature of 300 K and enables the most efficient absorption of energy waves generated by primary knock-out atoms (PKAs).[124] The size of thermostat region is chosen after trying thermostat regions of varying sizes. If the thermostat region is too large such that the thermostat atoms border the region under the electron irradiation too closely, reconstruction of the junction is inhibited due to the abrupt temperature differential in the system. For computational efficiency, rather than placing the CNTs on an atomistic substrate, the motion of atoms are simply limited to the space above the imaginary substrate placed below the tubes. To provide an accurate numerical integration in all simulations a time step of 0.2 fs is used.

The electron irradiation is mimicked by periodically assigning a velocity to a PKA. In general, when a large amount of kinetic energy is provided to an atom in a solid, this atom, the so-called PKA, generates an atomic collision cascade. The physical way of assigning of energies and momenta is based on the differential cross sectional areas derived from scattering theories.[163] However, this involves a significant fraction of "side

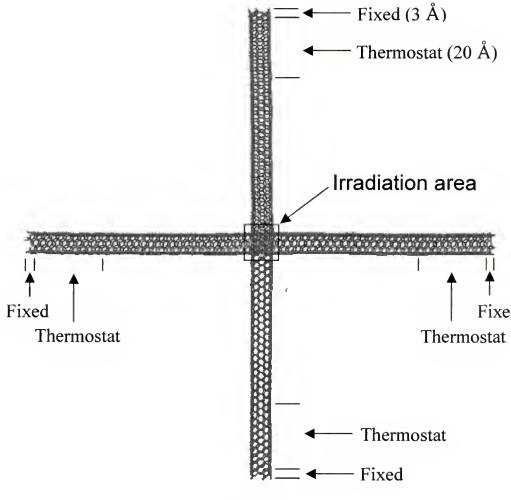

(a)Top view

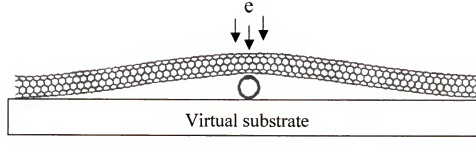

(b) Side view

Figure 4-1. Initial configuration of crossed nanotubes for electron beam irradiation.

collisions" with very little energy transfer. Limited by the small time scale of MD simulations, only collisions along the beam direction are incorporated, where the large energy transfer is predominantly, as is the momentum transfer. The kinetic energy assigned to the PKAs is 10 eV, which corresponds to "head on" collisions with an approximately 50 keV electron beam (due to low electron mass, only a fraction of its energy is transferred to the carbon atom) and is near the irradiation threshold for this model carbon nanotubes. All collisions between incoming electrons and PKAs are considered as elastic because energy loss can be ignored in this electron beam energy.[163] In these simulations, only high-energy transfer collisions are employed and there are a high frequency of these collisions. These conditions result in a very high local temperature at the junction which promotes annealing of the damage at faster rates than in experimental systems. Thus the procedure used, on the time scale of the MD simulations, is likely to heal defects rapidly.

Since the focus of these studies is on junction formation, only the atoms from the junction region are selected to be PKAs (see Figure 4-1). Also, to further accelerate the rate of structural changes and rebounding in this basic simulation cycle, one PKA every 10 MD steps for 2 ps is assigned, which is followed by 1 ps of cooling with no collisions to prevent the structure from melting or otherwise undergoing thermal dissociation. At the end of each 2 ps collision period, the average local temperature of the irradiated region is about 3500 K and this decreases to about 1600 K over the course of the cooling period. These temperatures are greater than those that occur in comparable experiments, where under irradiation in electron microscopes a steady temperature about 1000 K is more typical. However, these computational conditions greatly accelerate the simulations

and allows for reconstruction and rebonding to occur at the MD time scale, yet without melting, rapid collapse or other thermal degradation. For all junction formation simulations a total of 20 irradiation-cooling cycles is applied and followed by 20 ps of annealing at 600 K and a final cooling to 300 K.

It should be noted here that the empirical potential-based methods being used do not explicitly describe electrons but only considers charge neutral atomic systems. However, the effect of electron charge is included implicitly in the scattering event through the PKAs. As the corresponding irradiated experiment systems are sufficiently conducting, the charge of an incident beam will not accumulate but will be carried away from the impact site rapidly, justifying the use of charge-neutral models in these simulations.

The CNT junctions are formed between four pairs of crossed single-walled CNTs with the following chiral indices: (5,5)-(5,5), (10,0)-(10,0), (8,3)-(8,3), and (5,5)-(10,0), which all have similar diameters but different chiralities (the structural information is summarized in Table 4-1).

In order to investigate electronic properties of CNT junction, orthogonal tight binding (TB) model is used, which includes four valence orbitals $\{s, p_x, p_y, p_z\}$ for each carbon atom.[130] The electronic structure is obtained by analyzing the eigenvector

Table 4-1. The dimensions of each CNT pair and irradiation area.

	(5,5)-(5,5)	(10,0)-(10,0)	(8,3)-(8,3)	(5,5)-(10,0)
Diameter (Å)	7.5	7.9	7.8	7.5, 7.9
Length (Å)	162	161	165	162, 161
Irradiation Area ($Å^2$)	10 × 10	12 × 12	11 × 11	11 × 11

spectrum $c^{(n)}$ for the eigenvalues $\varepsilon^{(n)}$, $n \in 4N$, where N is the number of C atoms and $4N$ is the number of electrons in the supercell. The partial sum $\sum_n \left|c_\alpha^{(n)}(r_i)\right|^2$ is proportional to the probability density ("amplitude of the wavefunction") of the orbital α at the atomic site r_i, subject to the closure rule $\sum_n \sum_{i,\alpha} \left|c_\alpha^{(n)}(r_i)\right|^2 = 4N$. The "participation ratio", proportional to the second moment (mean) of the probability density, is defined as:

$$P^{(n)} = 4N \sum_{i,\alpha} \left|c_\alpha^{(n)}(r_i)\right|^4, \tag{4-1}$$

where the sum is running over all sites r_i and orbitals α. Its deviation from the ideal value $(4N)^{-1}$ gives an overall measure of the localization of the n-th eigenvalue.

This electronic structure computation is performed for only two CNT junctions, ideal (5,5)-(5,5) and e-beam irradiated (5,5)-(5,5) junctions. The total number of atoms is 568 and 340 for ideal (5,5)-(5,5) and e-beam irradiated (5,5)-(5,5) junctions, respectively. Periodic boundary condition is applied to the directions of two CNT axes and the structures are relaxed with TBMD at 0 K.

4.2 Results and Discussion

Figure 4-2 shows the final states of each CNT pair after annealing. In all four systems, the simulations predict a significant degree of covalent joining but not complete merging of the crossed CNTs. The resulting systems may represent partial junction formation due to very short simulation time, even taking into account "acceleration" schemes. However, the effective total dose in the simulations is quite large, and considering that transmission electron microscope images of electron-beam welded

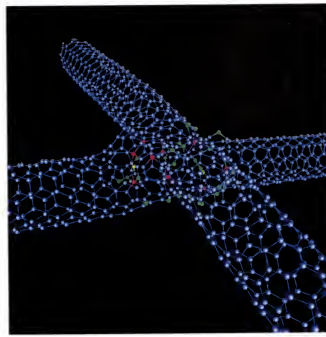

(a)

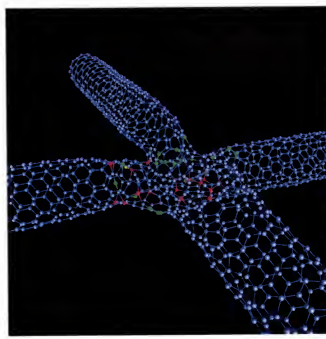

(b)

Figure 4-2. Final structure of each CNT pair after electron beam irradiation and annealing. Blue spheres represent sp^2 carbon atoms, pink spheres are sp^3 carbon atoms, green spheres are *sp* carbon atoms and yellow spheres are terminal carbon atoms. (a) (5,5)-(5,5), (b) (10,0)-(10,0), (c) (8,3)-(8,3), (d) (5,5)-(10,0)

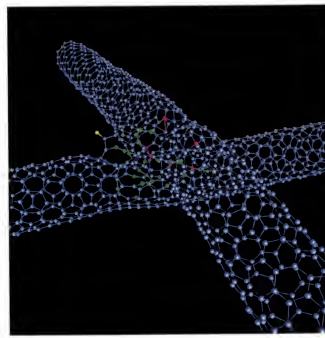

(c)

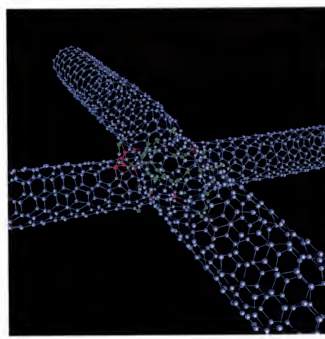

(d)

Figure 4-2. Continued.

junctions show rather "convoluted" structures, it is possible that models used in this simulation are better representations of real electron-welded junctions, rather than models of "ideal, epitaxial" junctions.

The simulations indicate that the chirality of the CNTs influences the merging process. The (5,5)-(5,5) pair shows better joining at the junction than the other pairs, while the irradiated region of the (10,0)-(10,0) pair shows CNT collapse and a decrease of the tube diameters, making the structure of this junction less smooth than the other pairs. The decrease of CNT diameters can be explained by imperfect reconstruction of the CNT surface after the displacement of atoms from the irradiation process. The (8,3)-(8,3) pair shows a structure that is intermediate between the structures of the (5,5)-(5,5) and (10,0)-(10,0) pairs. There is neither CNT collapse nor a noticeable decrease in nanotube diameters, but the joining at the junction is not as smooth as is the case for the (5,5)-(5,5) pair. Therefore, these simulations indicate that the reformation of hexagon and pentagon rings in junctions following electron irradiation occurs more readily in the (5,5)-(5,5) pair than any of the others considered. Interestingly, although the (10,0)-(10,0) pair is predicted to be the least favorable to joining by electron irradiation, the junction between the (5,5)-(10,0) pair is almost as smooth as that formed for the (5,5)-(5,5) pair and is significantly more smooth than the (10,0)-(10,0) pair. This finding may be explained by the complementary alignment of the hexagons in the two CNTs at the junction. It is also possible that in addition to the effects of chirality, the stochastic nature of the kinetic process affects the junction shape and quality in a non-systematic manner.

Table 4-2 summarizes the bonding properties of the carbon atoms around the junction region before and after annealing. The region analyzed is arbitrarily taken to be

Table 4-2. Summary of bonding at the junctions formed between the following pairs of CNTs by electron beam irradiation as described in the text.

	(5,5)-(5,5)		(10,0)-(10,0)		(8,3)-(8,3)		(5,5)-(10,0)	
	Before anneal	After anneal	Before anneal	After anneal	Before anneal	After anneal	Before anneal	After anneal
sp^3	1.9	3.2	2.4	4.5	3.3	1.9	2.4	3.0
sp^2	86.2	85.9	90.2	89.7	87.0	88.6	86.2	87.3
sp	10.3	10.3	6.7	5.5	8.9	9.1	10.8	9.2
Terminal	1.6	0.6	0.7	0.2	0.8	0.3	0.3	0.3

twice the length of the irradiation region. Therefore, only relative values are meaningful.

There are no large differences in the bonding between the various CNT pairs. However, the table shows that the (10,0)-(10,0) pair has significantly less *sp* bonding than the other pairs and more overall saturation of the junction carbon atoms. This might be associated with the collapse of the tube diameter described above.

Annealing increases the percentage of sp^3-hybridized atoms at the expense of the sp^2-hybridized and/or *sp*-hybridized atoms at all the junctions except for the one between the (8,3)-(8,3) CNTs. In this case, the percentage of sp^2 and *sp* carbon increases. This increased number of low coordinated atoms leads to a smaller number of joining bonds. In all other cases only reconstruction of atomic structure occurs. This difference in behavior might be because the (8,3) CNT junction is one path to dissociation into separate tubes. The number of terminal (dangling) carbon atoms at the junctions decreases during annealing for all CNT pairs except the (5,5)-(10,0) pair, perhaps because there were only a few terminal carbon atoms in this junction even before annealing.

All junctions formed in these simulations have a significant degree of bonding disorder. By contrast, to date the majority of junctions studied theoretically are constructed to minimize a number of bonding defects to provide the best connection possible between the tubes. It is likely that experimentally realized junctions under highly non-equilibrium synthesis conditions will not be "ideal". It is therefore interesting to analyze the effect of the junction structure on various properties and compare them with those of the reference "ideal" junction.

To characterize the mechanical responses of the synthesized junctions, they are deformed in tension and compression as illustrated in the schematics in Figure 3. For these tests, the welded CNTs are shortened to 40 Å in order to magnify the effect of the junction region and the two deformation modes were carried out by moving the rigid ends of the CNTs either apart or towards each other at a constant velocity of 10 m/s. In addition to the four junctions described above, an ideally merged (5,5)-(5,5) pair and hydrogen terminated (5,5)-(5,5) pair are also tested for comparison. The ideal junction

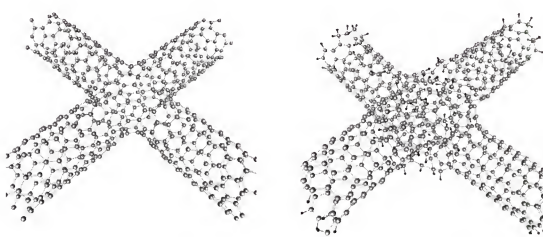

(a) (b)

Figure 4-3. Structure models of (a) ideal (5,5)-(5,5) CNT junction and (b) hydrogen terminated (5,5)-(5,5) CNT junction. Small black spheres are hydrogen atoms.

between the (5,5)-(5,5) pair is made by artificially manipulating the atoms in the junction region, while the hydrogen terminated (5,5)-(5,5) pair is prepared by capping the active sites in the electron irradiated (5,5)-(5,5) pair junction with hydrogen atoms (see Figure 4-3).

Figure 4-4(a) shows the total energy of the junction structure as a function of tensile strain for three different (5,5)-(5,5) junctions. The irradiation welded (5,5)-(5,5) junctions exhibit a behavior typical of all the irradiated junctions considered in this study.

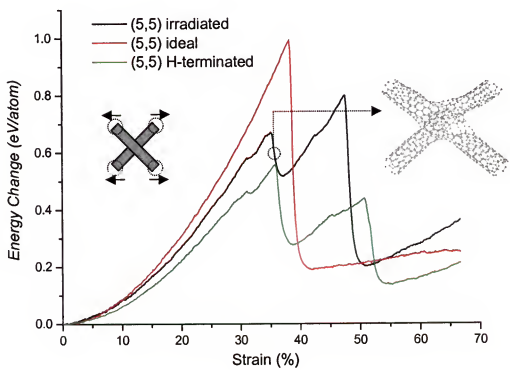

(a)

Figure 4-4. The change in energy as a function of strain during the deformation of welded CNT pairs after annealing. Each deformation mode is depicted in a schematic inset in the figure, and atomic structures for after large deformation are also shown.

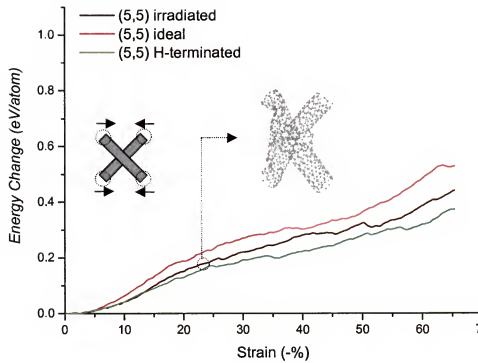

(b)

Figure 4-4. Continued.

There is an initial parabolic energy dependence on the strain corresponding to elastic loading followed by rapid elastic energy release associated with an irreversible bond breaking dissipative process. Remaining and newly formed bonds lead to a second elastic loading stage followed by another bond breaking event. Depending on the junction, this process might repeat itself several times until the junction is completely broken. In the case of the ideal junction, there is only one, high-energy peak that corresponds to atomic deformation in response to the applied forces. This peak is higher than in any other cased, indicating that this is the strongest and stiffest junction of those considered here. However, the ideal junction is more brittle and after the initial failure does not support any load. This behavior is consistent with typical mechanical behavior, where an increase

in strength is accompanied by a decrease in ductility. Interestingly, the hydrogen termination of the irradiated junction leads to softening and weakening of the junction, with a slight increase in ductility. These effects are attributed to the fact that the hydrogen termination effectively weakens neighboring bonds to the H-terminated C atom due to changes in hybridization. Similar behavior is observed for the compressive deformation mode described below. The most significant difference between the tensile and compressive "scissoring" deformation (see Fig 4-4(b)), is in the facts that there are no abrupt energy releases. This a consequence of bond rearrangement, rather than bond fracture, dominating the plastic deformation process under compressive load.

Figure 4-5 shows the total density of state (DOS) of the ideal (5,5)-(5,5) junction

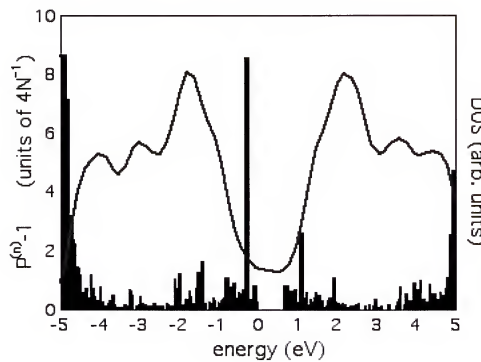

Figure 4-5. DOS (full curve) and eigenvalue participation ratio (histogram) around the Fermi level (shifted at $E = 0$) for ideal (5,5)-(5,5) CNT junction.

(full curve) and the participation ratio $P^{(n)}$ (histogram) around the Fermi level $E_F = 0$ eV. The DOS remains quite flat around the Fermi level. No sign of localization is apparent for an extent of about 0.5 eV above E_F, while a moderate localization is seen for a few "shallow" states lying immediately below E_F. This implies that the structural defects induce only a moderate perturbation on the conduction-electron wavefunctions. In addition, the atomic structure still preserves several connecting paths across all the four branches of the cross. Therefore, it is expected that good ohmic conduction is preserved in this CNT junction though there is moderate concentration of topological and coordination defects and localized energy states.

The electronic structure of (5,5)-(5,5) junction produced by electron beam irradiation is very interesting (shown in Figure 4-6). A whole band around the

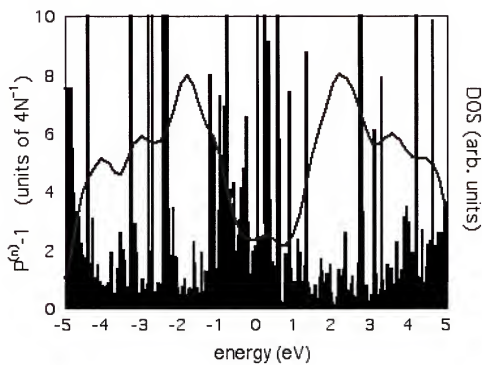

Figure 4-6. DOS and eigenvalue participation ratio around the Fermi level for (5,5)-(5,5) CNT junction produced by electron beam irradiation.

Fermi level is localized at the junction region. All the energy levels are quantized within the junction, although being finely spaced by $\Delta E \approx 10$ -50 meV. Such levels are defect states, but are weakly localized (i.e., spread) over the whole of the junction sites, while not belonging to the rest of the system. This can be clearly seen by plotting the quantity $\sum_\alpha \left|c_\alpha^{(n)}(x_i)\right|^2$ as a function of the distance x_i, spanning either major axis of the cross. Figure 4-7 shows such plots for the first few eigenvalues of the discrete spectrum (n=1,2, …, 8) above the Fermi level (n = 0). For n = 0, 1 the wavefunction is moderately

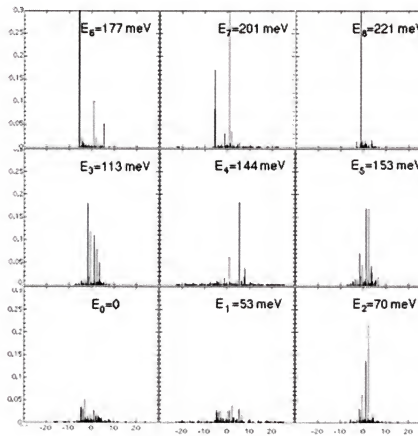

Figure 4-7. Plot of the longitudinal distribution of the electron probability density, $\sum_\alpha \left|c_\alpha^{(n)}(x)\right|^2$, for the first few eigenvalues (n=0,...8) above the Fermi level (n=0) of the (5,5)-(5,5) CNT junction produced by electron beam irradiation. The abscissa x spans either of the major tube axes. The junction region lies approximately between x=-5 Å and x=+5 Å.

localized, and spreads over the rest part of the system. In contrast, the wavefunctions are substantially different from the case of $n = 0$ in the junction region for $n \geq 2$. In some cases wavefunctions are more strongly localized just at a few atomic sites. The combination of energy quantization and spatial localization observed in this junction is the typical signature of a quantum dot (QD).

4.3 Conclusions

This simulation study demonstrated that under appropriate selection of simulation parameters, MD simulations are capable of mimicking the process of covalent junction formation between carbon nanotubes. The structure of generated junctions is characterized by a large degree of bonding disorder that leads to lower strength and higher ductility than those characterizing "ideal" junctions. The level of disorder at the junction can be in part a consequence of the small time scale of these classical MD simulations, even taking into account the "accelerating" procedures used in this work. However, such disorder is likely to be present in CNT junctions synthesized under highly non-equilibrium conditions. Finally it is noted that the structures generated in these simulations appear visually to less defective than those generated recently via simulated ion irradiation.[109] Possible reasons for this can be the fact that these electron beam simulations are operated near the irradiation threshold with each collision leading to much more localized damage than is the case with bombardment with energetic ions, which involves much higher energy transfers leading to more extended damage.

Electronic structure investigation shows the CNT junctions produced by electron beam irradiation have an interesting QD characteristics. From that prediction, it is expected that the arrays of all-carbon-based QDs as small as 1 nm, spaced by 5-10 nm can be realized. Such QDs would have capabilities of all-carbon based nanoelectronic

devices and can be used as building blocks of more complex molecular-scale electronic circuits.

CHAPTER 5
GENERAL CONCLUSIONS

In the studies described in this dissertation, detailed information of reaction mechanisms and structural changes in polyatomic ion deposition and carbon nanotube welding processes are explored with molecular dynamics simulation. The kind of information provided by the simulations, such as bonding characteristics in carbon nanotube junctions produced by electron irradiation and detailed reaction mechanisms between incident polyatomic ions and polymer surfaces in plasma deposition, are exclusively provided by molecular simulation studies and are difficult to obtain with experimental methods. While the predictions provided by these simulation studies might not be as quantitatively accurate as *ab-initio* calculation methods, they have the advantage of providing insight into the atomic scale processes that occur in large complex and delicate systems.

The studies of continuous fluorocarbon ion deposition on PS surface show how and why CF_3^+ and $C_3F_5^+$ play different roles in plasma deposition processes on hydrocarbon polymers. CF_3^+ ions dissociate more readily on impact and the large number of F atoms that are produced form covalent bonds with the PS chains, which both efficiently fluorinates the PS and slows down thin film growth. In contrast, $C_3F_5^+$ ions produce more fluorocarbon polymer film precursors that enhance thin film growth, while at the same time fluorinating the surface at a slower rate. Additionally, it can be suggested that CF_2 is likely to be an important precursor for film growth from fluorocarbon polyatomic ions, in general.

In the study of hydrocarbon ion deposition on polymer substrates, it is shown that deposition at an inclined angle such as 45° should be more efficient for shallow surface modification than normal incidence even though more scattering takes place. Also, compared with the results of depositions at 25 eV incident energy of ion, 50 eV depositions are more effective. When PS and PE substrates are compared with each other, more ions dissociate and remain on the PS surface, and more ions and fragments remain in a shallow region of the PS surface than PE surface. However, the amount of total carbon deposited on the PE surface is not much smaller than the amount deposited on the PS surface. The amount of major fragments (C_2H_n and CH_2) deposited on both surfaces at 50 eV is almost the same. A minor property of the PE substrate is that relatively more carbon-carbon bonds are broken by ion deposition on the PE surface than on the PS surface.

In the study of carbon nanotube welding, the structure of generated junctions is characterized by a large degree of bonding disorder that leads to lower strength and higher ductility than those characterizing "ideal" junctions. Such disorder is likely to be present in carbon nanotube junctions synthesized under highly non-equilibrium conditions. Also it is noted that the structures generated in these simulations appear visually to be less defective than those generated recently via simulated ion irradiation. Electronic structure analysis reveals that carbon nanotube junctions produced by electron beam irradiation have an interesting quantum dot (QD) characteristics. From that prediction, it is expected that the arrays of all-carbon-based QDs as small as 1 nm, spaced by 5-10 nm can be realized. Such QDs would have capabilities of all-carbon based

nanoelectronic devices and can be used as building blocks of more complex molecular-scale electronic circuits.

LIST OF REFERENCES

1. D. Frenkel and S. Berend, Understanding Molecular Simulation, Academic Press, New York, 1996.

2. M. B. J. Wijesundara, L. Hanley, B. R. Ni, and S. B. Sinnott, Proceedings of the National Academy of Sciences of the United States of America, **97**, 23 (2000).

3. M. B. J. Wijesundara, Y. Ji, B. Ni, S. B. Sinnott, and L. Hanley, Journal of Applied Physics, **88**, 5004 (2000).

4. I. Jang, B. Ni, and S. B. Sinnott, Journal of Vacuum Science & Technology A, **20**, 564 (2002).

5. I. Jang, R. Phillips, and S. B. Sinnott, Journal of Applied Physics, **92**, 3363 (2002).

6. C. F. Abrams and D. B. Graves, Journal of Vacuum Science & Technology A, **19**, 175 (2001).

7. D. R. Alfonso and S. E. Ulloa, Physical Review B, **48**, 12235 (1993).

8. S. Ramalingam, D. Maroudas, and E. S. Aydil, Journal of Applied Physics, **86**, 2872 (1999).

9. P. B. Balbuena and J. M. Seminario, Molecular Dynamics : From Classical to Quantum Methods, Elsevier, New York, 1999.

10. D. C. Young, Computational Chemistry : A Practical Guide for Applying Techniques to Real World Problems, Wiley, New York, 2001.

11. B. J. Alder and T. E. Wainwright, Journal of Chemical Physics, **31**, 459 (1959).

12. B. J. Alder and T. E. Wainwright, Journal of Chemical Physics, **27**, 1208 (1957).

13. F. H. Stillinger and A. Rahman, Journal of Chemical Physics, **60**, 1545 (1974).

14. D. C. Gray, V. Mohindra, and H. H. Sawin, Journal of Vacuum Science & Technology A, **12**, 354 (1994).

15. A. Partridge, P. Harris, T. Hirotsu, and S. Kurosawa, Plasmas and Polymers, **5**, 191 (2000).

16. R. L. Kostelak, T. W. Weidman, S. Vaidya, O. Joubert, S. C. Palmateer, and M. Hibbs, Journal of Vacuum Science & Technology B, **13**, 2994 (1995).

17. F. F. Shi, Surface and Coatings Technology, **82**, 1 (1996).

18. C.-M. Chan, T.-M. Ko, and H. Hiraoka, Surface Science Reports, **24**, 1 (1996).

19. C.-M. Chan, Polymer Surface Modification and Characterization, Hanser/Gardner, New York, 1994.

20. G. Kuhn, I. Retzko, A. Lippitz, W. Unger, and J. Friedrich, Surface & Coatings Technology, **142**, 494 (2001).

21. P. Favia and R. d'Agostino, Vide-Science Technique Et Applications, **57**, 40 (2002).

22. J. X. Tang, S. Li, Z. C. Liu, L. B. Nie, P. F. Xiao, Z. H. Lu, and N. Y. He, Acta Chimica Sinica, **61**, 641 (2003).

23. D. S. Wavhal and E. R. Fisher, Journal of Polymer Science Part B-Polymer Physics, **40**, 2473 (2002).

24. S. K. Oiseth, A. Krozer, B. Kasemo, and J. Lausmaa, Applied Surface Science, **202**, 92 (2002).

25. M. Tahara, N. K. Cuong, and Y. Nakashima, Surface & Coatings Technology, **174**, 826 (2003).

26. M. E. H. M. da Costa, J. Freire, F. L., L. G. Jacobsohn, D. Franceschini, G. Mariotto, and I. R. J. Baumvol, Diamond and Related Materials, **10**, 910 (2001).

27. H. Biederman, Vacuum, **59**, 594 (2000).

28. H. Yasuda, Plasma polymerization, Academic Press, Orlando, 1985.

29. A. von Keudell, Thin Solid Films, **402**, 1 (2002).

30. H. Yang and W. J. van Ooij, Plasmas and Polymers, **8**, 297 (2003).

31. G. H. Yang, Y. Zhang, E. T. Kang, and K. G. Neoh, Journal of Physical Chemistry B, **107**, 2780 (2003).

32. T. M. Mayer, R. A. Barker, and L. J. Whitman, Journal of vacuum Science & Technology, **18**, 349 (1981).

33. J. W. Butterbaugh, D. C. Gray, and H. H. Sawin, Journal of Vacuum Science & Technology B, **9**, 1461 (1991).

34. M. T. Kim, Journal of the Electrochemical Society, **150**, G683 (2003).

35. X. Y. Lu, Z. S. Jin, S. Q. Hao, H. Y. Peng, and Q. Z. Cao, New Carbon Materials, **18**, 191 (2003).

36. J. H. Wang, J. J. Chen, and R. B. Timmons, Chemistry of Materials, **8**, 2212 (1996).

37. B. O. Cho, S. W. Hwang, G. R. Lee, and S. H. Moon, Journal of Vacuum Science & Technology A, **19**, 730 (2001).

38. K. Takahashi, A. Itoh, T. Nakamura, and K. Tachibana, Thin Solid Films, **374**, 303 (2000).

39. M. Horie, Journal of Vacuum Science & Technology a-Vacuum Surfaces and Films, **13**, 2490 (1995).

40. R. Dagostino, F. Cramarossa, V. Colaprico, and R. Dettole, Journal of Applied Physics, **54**, 1284 (1983).

41. I. H. Loh, M. Klausner, R. F. Baddour, and R. E. Cohen, Polymer Engineering and Science, **27**, 861 (1987).

42. M. Strobel, S. Corn, C. S. Lyons, and G. A. Korba, Journal of Polymer Science Part A, **23**, 1125 (1985).

43. H. Y. Kim and H. K. Yasuda, Journal of Vacuum Science & Technology A, **15**, 1837 (1997).

44. H. U. Poll and S. Schreiter, Surface & Coatings Technology, **93**, 105 (1997).

45. D. W. Brenner and J. A. Harrison, American Ceramic Society Bulletin, **71**, 1821 (1992).

46. G. S. Oehrlein, Y. Zhang, D. Vender, and M. Haverlag, Journal of Vacuum Science & Technology A, **12**, 323 (1994).

47. C. F. Abrams and D. B. Graves, Journal of Applied Physics, **86**, 5938 (1999).

48. I. Bello, W. H. Chang, and W. M. Lau, Journal of Vacuum Science & Technology A, **12**, 1425 (1994).

49. C. A. Nichols, J. R. Woodworth, and T. W. Hamilton, Journal of Vacuum Science & Technology a-Vacuum Surfaces and Films, **16**, 3389 (1998).

50. H. K. Hu and J. W. Rabalais, Journal of Physical Chemistry, **85**, 2459 (1981).

51. B. A. Helmer and D. B. Graves, Journal of Vacuum Science & Technology A, **15**, 2252 (1997).

52. L. R. Williston, I. Bello, and W. M. Lau, Journal of Vacuum Science & Technology A, **10**, 1365 (1992).

53. Y. Y. Tu, T. J. Chuang, and H. F. Winters, Physical Review B, **23**, 823 (1981).

54. R. J. Fessenden and J. S. Fessenden, Organic Chemistry, Brooks/Cole, Pacific Grove, California, 1990.

55. P. M. Ajayan, Chemical Reviews, **99**, 1787 (1999).

56. J. W. Mintmire, B. I. Dunlap, and C. T. White, Physical Review Letters, **68**, 631 (1992).

57. N. Hamada, S. Sawada, and A. Oshiyama, Physical Review Letters, **68**, 1579 (1992).

58. M. S. Dresselhaus, G. Dresselhaus, and P. Avouris, Carbon Nanotubes : Synthesis, Structure, Properties, and Applications, Springer, New York, 2001.

59. S. Iijima, Nature, **354**, 56 (1991).

60. D. S. Bethune, C. H. Kiang, M. S. Devries, G. Gorman, R. Savoy, J. Vazquez, and R. Beyers, Nature, **363**, 605 (1993).

61. S. Iijima and T. Ichihashi, Nature, **363**, 603 (1993).

62. C. H. Kiang, W. A. Goddard, R. Beyers, and D. S. Bethune, Carbon, **33**, 903 (1995).

63. C. Journet, W. K. Maser, P. Bernier, A. Loiseau, M. L. delaChapelle, S. Lefrant, P. Deniard, R. Lee, and J. E. Fischer, Nature, **388**, 756 (1997).

64. A. Thess, R. Lee, P. Nikolaev, H. J. Dai, P. Petit, J. Robert, C. H. Xu, Y. H. Lee, S. G. Kim, A. G. Rinzler, D. T. Colbert, G. E. Scuseria, D. Tomanek, J. E. Fischer, and R. E. Smalley, Science, **273**, 483 (1996).

65. B. I. Yakobson, C. J. Brabec, and J. Bernholc, Physical Review Letters, **76**, 2511 (1996).

66. E. W. Wong, P. E. Sheehan, and C. M. Lieber, Science, **277**, 1971 (1997).

67. L. Langer, V. Bayot, E. Grivei, J. P. Issi, J. P. Heremans, C. H. Olk, L. Stockman, C. VanHaesendonck, and Y. Bruynseraede, Physical Review Letters, **76**, 479 (1996).

68. H. J. Dai, E. W. Wong, and C. M. Lieber, Science, **272**, 523 (1996).

69. T. W. Ebbesen, H. J. Lezec, H. Hiura, J. W. Bennett, H. F. Ghaemi, and T. Thio, Nature, **382**, 54 (1996).

70. P. M. Ajayan, T. W. Ebbesen, T. Ichihashi, S. Iijima, K. Tanigaki, and H. Hiura, Nature, **362**, 522 (1993).

71. S. C. Tsang, P. J. F. Harris, and M. L. H. Green, Nature, **362**, 520 (1993).

72. P. M. Ajayan, L. S. Schadler, C. Giannaris, and A. Rubio, Advanced Materials, **12**, 750 (2000).

73. S. Curran, A. P. Davey, J. Coleman, A. Dalton, B. McCarthy, S. Maier, A. Drury, D. Gray, M. Brennan, K. Ryder, M. L. de la Chapelle, C. Journet, P. Bernier, H. J. Byrne, D. Carroll, P. M. Ajayan, S. Lefrant, and W. Blau, Synthetic Metals, **103**, 2559 (1999).

74. C. Nutzenadel, A. Zuttel, D. Chartouni, and L. Schlapbach, Electrochemical and Solid State Letters, **2**, 30 (1999).

75. G. Treboux, P. Lapstun, and K. Silverbrook, Journal of Physical Chemistry B, **103**, 1871 (1999).

76. S. S. Wong, E. Joselevich, A. T. Woolley, C. L. Cheung, and C. M. Lieber, Nature, **394**, 52 (1998).

77. S. J. Tans, A. R. M. Verschueren, and C. Dekker, Nature, **393**, 49 (1998).

78. H. D. Wagner, O. Lourie, Y. Feldman, and R. Tenne, Applied Physics Letters, **72**, 188 (1998).

79. L. Chico, V. H. Crespi, L. X. Benedict, S. G. Louie, and M. L. Cohen, Physical Review Letters, **76**, 971 (1996).

80. J. W. Mintmire and C. T. White, Synthetic Metals, **77**, 231 (1996).

81. K. Tsukagoshi, N. Yoneya, S. Uryu, Y. Aoyagi, A. Kanda, Y. Ootuka, and B. W. Alphenaar, Physica B: Condensed Matter, **323**, 107 (2002).

82. P. Avouris, Chemical Physics, **281**, 429 (2002).

83. H. Dai, Surface Science, **500**, 218 (2002).

84. H. W. C. Postma, T. Teepen, Z. Yao, M. Grifoni, and C. Dekker, Science, **293**, 76 (2001).

85. Z. Yao, H. W. C. Postma, L. Balents, and C. Dekker, Nature, **402**, 273 (1999).

86. J. Kong, J. Cao, H. J. Dai, and E. Anderson, Applied Physics Letters, **80**, 73 (2002).

87. J. Kong and H. J. Dai, Journal of Physical Chemistry B, **105**, 2890 (2001).

88. A. N. Andriotis, M. Menon, D. Srivastava, and L. Chernozatonskii, Physical Review Letters, **8706**, 066802 (2001).

89. M. Menon and D. Srivastava, Physical Review Letters, **79**, 4453 (1997).

90. C. G. Rocha, T. G. Dargam, and A. Latge, Physical Review B, **65**, 165431 (2002).

91. L. Chico, M. P. L. Sancho, and M. C. Munoz, Physical Review Letters, **81**, 1278 (1998).

92. A. N. Andriotis, M. Menon, D. Srivastava, and L. Chernozatonskii, Physical Review B, **65**, 165416 (2002).

93. J. Kim, J. O. Lee, H. Oh, K. H. Yoo, and J. J. Kim, Physical Review B, **6416**, 161404 (2001).

94. V. Meunier, M. B. Nardelli, J. Bernholc, T. Zacharia, and J. C. Charlier, Applied Physics Letters, **81**, 5234 (2002).

95. A. Rochefort and P. Avouris, Nano Letters, **2**, 253 (2002).

96. R. Tamura, Physical Review B, **6420**, 201404 (2001).

97. J. O. Lee, H. Oh, J. R. Kim, K. Kang, J. J. Kim, J. Kim, and K. H. Yoo, Applied Physics Letters, **79**, 1351 (2001).

98. A. N. Andriotis, M. Menon, D. Srivastava, and L. Chernozatonskii, Applied Physics Letters, **79**, 266 (2001).

99. M. S. Ferreira, T. G. Dargam, R. B. Muniz, and A. Latge, Physical Review B, **62**, 16040 (2000).

100. A. A. Odintsov, Physical Review Letters, **85**, 150 (2000).

101. A. A. Farajian, K. Esfarjani, and Y. Kawazoe, Physical Review Letters, **82**, 5084 (1999).

102. R. Tamura and M. Tsukada, Physical Review B, **55**, 4991 (1997).

103. M. Terrones, F. Banhart, N. Grobert, J. C. Charlier, H. Terrones, and P. M. Ajayan, Physical Review Letters, **89**, 075505 (2002).

104. F. Banhart, Nano Letters, **1**, 329 (2001).

105. H. W. C. Postma, M. de Jonge, Z. Yao, and C. Dekker, Physical Review B, **62**, 10653 (2000).

106. P. W. Chiu, G. S. Duesberg, U. Dettlaff-Weglikowska, and S. Roth, Applied Physics Letters, **80**, 3811 (2002).

107. B. Ni, R. Andrews, D. Jacques, D. Qian, M. B. J. Wijesundara, Y. S. Choi, L. Hanley, and S. B. Sinnott, Journal of Physical Chemistry B, **105**, 12719 (2001).

108. K. Metenier, S. Bonnamy, F. Beguin, C. Journet, P. Bernier, M. L. de La Chapelle, O. Chauvet, and S. Lefrant, Carbon, **40**, 1765 (2002).

109. A. V. Krasheninnikov, K. Nordlund, J. Keinonen, and F. Banhart, Physical Review B, **66**, 245403 (2002).

110. J. Tersoff, Physical Review B, **37**, 6991 (1988).

111. J. Tersoff, Physical Review B, **38**, 9902 (1988).

112. J. Tersoff, Physical Review B, **39**, 5566 (1989).

113. G. C. Abell, Physical Review B, **31**, 6184 (1985).

114. D. W. Brenner, Physical Review B: Condensed Matter, **42**, 9458 (1990).

115. D. W. Brenner, Physica Status Solidi B-Basic Research, **217**, 23 (2000).

116. D. W. Brenner, O. A. Shenderova, J. A. Harrison, S. J. Stuart, B. Ni, and S. B. Sinnott, Journal of Physics-Condensed Matter, **14**, 783 (2002).

117. E. R. Williams, G. C. Jones, L. Fang, R. N. Zare, B. J. Garrison, and D. W. Brenner, Journal of the American Chemical Society, **114**, 3207 (1992).

118. L. F. Qi and S. B. Sinnott, Journal of Vacuum Science & Technology A, **16**, 1293 (1998).

119. D. R. Alfonso, S. E. Ulloa, and D. W. Brenner, Physical Review B, **49**, 4948 (1994).

120. D. W. Brenner, J. A. Harrison, C. T. White, and R. J. Colton, Thin Solid Films, **206**, 220 (1991).

121. J. Tanaka, C. F. Abrams, and D. B. Graves, Journal of Vacuum Science & Technology A, **18**, 938 (2000).

122. M. J. S. Dewar and E. G. Zoebisch, Theochem-Journal of Molecular Structure, **49**, 1 (1988).

123. M. J. S. Dewar, E. G. Zoebisch, E. F. Healy, and J. J. P. Stewart, Journal of the American Chemical Society, **107**, 3902 (1985).

124. M. P. Allen and D. J. Tildesley, Computer simulation of liquids, Oxford University Press, New York, 1987.

125. N. Bernstein and E. Kaxiras, Physical Review B, **56**, 10488 (1997).

126. G. Galli, Computational Materials Science, **12**, 242 (1998).

127. P. D. Godwin, A. K. Roberts, D. Yu, K. Dean, and P. Clancy, Computational Materials Science, **21**, 135 (2001).

128. L. J. Lewis and N. Mousseau, Computational Materials Science, **12**, 210 (1998).

129. M. Menon and K. R. Subbaswamy, Physical Review B, **47**, 12754 (1993).

130. C. H. Xu, C. Z. Wang, C. T. Chan, and K. M. Ho, Journal of Physics-Condensed Matter, **4**, 6047 (1992).

131. M. Menon and K. R. Subbaswamy, Physical Review B, **50**, 11577 (1994).

132. E. T. Ada, O. Kornienko, and L. Hanley, Journal of Physical Chemistry B, **102**, 3959 (1998).

133. L. R. Williston, I. Bello, and W. M. Lau, Journal of Vacuum Science & Technology A, **11**, 1242 (1993).

134. C. F. Abrams and D. B. Graves, Thin Solid Films, **374**, 150 (2000).

135. C. F. Abrams and D. B. Graves, Journal of Applied Physics, **88**, 3734 (2000).

136. R. Smith and K. Beardmore, Thin Solid Films, **272**, 255 (1996).

137. S. Ramalingam, D. Maroudas, and E. S. Aydil, Journal of Applied Physics, **84**, 3895 (1998).

138. S. Ramalingam, D. Maroudas, and E. S. Aydil, Applied Physics Letters, **72**, 578 (1998).

139. P. M. DeLuca, K. C. Ruthe, and S. A. Barnett, Physical Review Letters, **86**, 260 (2001).

140. F. J. Palacios, M. P. Iniguez, M. J. Lopez, and J. A. Alonso, Physical Review B, **62**, 16031 (2000).

141. S. van Dijken, L. C. Jorritsma, and B. Poelsema, Physical Review B, **61**, 14047 (2000).

142. M. Moseler, O. Rattunde, J. Nordiek, and H. Haberland, Nuclear Instruments & Methods in Physics Research Section B-Beam Interactions with Materials and Atoms, **164**, 522 (2000).

143. S. Abdollahi-Alibeik, J. P. McVittie, K. C. Saraswat, V. Sukharev, and P. Schoenborn, Journal of Vacuum Science & Technology A, **17**, 2485 (1999).

144. B. Abraham-Shrauner and N. Jagannathan, Ieee Transactions on Plasma Science, **27**, 668 (1999).

145. S. W. Levine, J. R. Engstrom, and P. Clancy, Surface Science, **401**, 112 (1998).

146. T. Ohashi, K. Miyake, and K. Ohashi, Nuclear Instruments & Methods in Physics Research Section B-Beam Interactions with Materials and Atoms, **121**, 40 (1997).

147. C. Hedlund, C. Strandman, I. V. Katardjiev, Y. Backlund, S. Berg, and H. O. Blom, Journal of Vacuum Science & Technology B, **14**, 3239 (1996).

148. A. M. Barklund and H. O. Blom, Journal of Vacuum Science & Technology A, **10**, 1212 (1992).

149. D. P. Hamblen and A. Chalin, Journal of the Electrochemical Society, **135**, 1816 (1988).

150. S. Matsui, T. Yamato, H. Aritome, and S. Namba, Japanese Journal of Applied Physics, **19**, L126 (1980).

151. L. H. Sperling, Introduction to physical polymer science, Wiley, New York, 1992.

152. D. C. Gray, H. H. Sawin, and J. W. Butterbaugh, Journal of Vacuum Science & Technology A, **9**, 779 (1991).

153. N. M. Mackie, V. A. Venturo, and E. R. Fisher, Journal of Physical Chemistry B, **101**, 9425 (1997).

154. M. Inayoshi, M. Ito, M. Hori, T. Goto, and M. Hiramatsu, Journal of Vacuum Science & Technology A, **16**, 233 (1998).

155. M. Nakamura, M. Hori, T. Goto, M. Ito, and N. Ishii, Journal of Vacuum Science & Technology, A: Vacuum, Surfaces, and Films, **19**, 2134 (2001).

156. G. Cunge and J. P. Booth, Journal of Applied Physics, **85**, 3952 (1999).

157. W. R. Koppers, M. A. Gleeson, J. Lourenco, T. L. Weeding, J. Los, and A. W. Kleyn, Journal of Chemical Physics, **110**, 2588 (1999).

158. W. R. Koppers, J. H. M. Beijersbergen, T. L. Weeding, P. G. Kistemaker, and A. W. Kleyn, Journal of Chemical Physics, **107**, 10736 (1997).

159. T. Ast, D. E. Riederer, S. A. Miller, M. Morris, and R. G. Cooks, Organic Mass Spectrometry, **28**, 1021 (1993).

160. E. H. Lee, G. R. Rao, and L. K. Mansur, Materials Science Applications of Ion Beam Techniques, **248-249**, 135 (1997).

161. L. Hanley, H. Lim, D. G. Schultz, S. B. Wainhaus, P. deSainteClaire, and W. L. Hase, Nuclear Instruments & Methods in Physics Research Section B-Beam Interactions with Materials and Atoms, **125**, 218 (1997).

162. D. G. Schultz, S. B. Wainhaus, L. Hanley, P. deSainteClaire, and W. L. Hase, Journal of Chemical Physics, **106**, 10337 (1997).

163. S. V. Starodubtsev and A. M. Romanov, The Passage of Charged Particles through Matter, Academy of Sciences of the Uzbek SSR, Tashkent, 1962.

BIOGRAPHICAL SKETCH

Inkook Jang was born in Seoul, Korea, in 1972. He received his B.S. and M.S. degree in chemical engineering at Seoul National University, Korea, in 1995 and 1997, respectively. After two years of military service in Korean army, he started his study for Ph. D. degree in the Department of Materials Science and Engineering at University of Florida in 2000. His research has been focused on molecular simulation studies of material modification. Since 2002, he has been a member of the American Vacuum Society and he received an Honorable Mention in Physical Science in the 2003 Joint Symposium of the Florida Chapter of the American Vacuum Society and the Florida Society for Microscopy.

I certify that I have read this study and that in my opinion it conforms to acceptable standards of scholarly presentation and is fully adequate, in scope and quality, as a dissertation for the degree of Doctor of Philosophy.

Susan B. Sinnott, Chair
Associate Professor of Materials Science and Engineering

I certify that I have read this study and that in my opinion it conforms to acceptable standards of scholarly presentation and is fully adequate, in scope and quality, as a dissertation for the degree of Doctor of Philosophy.

Simon R. Phillpot
Professor of Materials Science and Engineering

I certify that I have read this study and that in my opinion it conforms to acceptable standards of scholarly presentation and is fully adequate, in scope and quality, as a dissertation for the degree of Doctor of Philosophy.

Laurie Gower
Associate Professor of Materials Science and Engineering

I certify that I have read this study and that in my opinion it conforms to acceptable standards of scholarly presentation and is fully adequate, in scope and quality, as a dissertation for the degree of Doctor of Philosophy.

Wolfgang Sigmund
Associate Professor of Materials Science and Engineering

I certify that I have read this study and that in my opinion it conforms to acceptable standards of scholarly presentation and is fully adequate, in scope and quality, as a dissertation for the degree of Doctor of Philosophy.

Rodney J. Bartlett
Graduate Research Professor of Chemistry and Physics

This dissertation was submitted to the Graduate Faculty of the College of Engineering and to the Graduate School and was accepted as partial fulfillment of the requirements for the degree of Doctor of Philosophy.

May 2004

Pramod P. Khargonekar
Dean, College of Engineering

Winfred M. Phillips
Dean, Graduate School